Pre-fusion AAA+ remodeling of target-SNARE protein complexes enables synaptic transmission

K. Ian White[1,2,3,4,5,**], Yousuf A. Khan[1,2,3,4,5], Kangqiang Qiu[6], Ashwin Balaji[7], Sergio Couoh-Cardel[1,2,3,4,5], Luis Esquivies[1,2,3,4,5], Richard A. Pfuetzner[1,2,3,4,5], Jiajie Diao[6], Axel T. Brunger[1,2,3,4,5,8,*]

[1]Department of Molecular and Cellular Physiology, Stanford University, Stanford, California, United States
[2]Department of Neurology and Neurological Sciences, Stanford University, Stanford, California, United States
[3]Department of Structural Biology, Stanford University, Stanford, California, United States
[4]Department of Photon Science, Stanford University, Stanford, California, United States
[5]Howard Hughes Medical Institute, Stanford University, Stanford, California, United States
[6]Department of Cancer Biology, University of Cincinnati College of Medicine, Cincinnati, United States
[7]Department of Chemistry, Stanford University, Stanford, California, United States
[8]Lead contact

[*]Correspondence: brunger@stanford.edu
[**]Correspondence: kiwhite@stanford.edu

Keywords

Membrane vesicle trafficking, AAA+ protein; neurotransmitter release; synapse; nanocluster; active zone; syntaxin; SNAP-25; NSF; ATP; hydrolysis

Summary

Membrane fusion is driven by SNARE complex formation across cellular contexts, including vesicle fusion during synaptic transmission. Multiple proteins organize trans-SNARE complex assembly and priming, leading to fusion. One target membrane SNARE, syntaxin, forms nanodomains at the active zone, and another, SNAP-25, enters non-fusogenic complexes with it. Here, we show that the AAA+ protein NSF (N-ethylmaleimide sensitive factor) and SNAP (soluble NSF attachment protein) must act prior to fusion. We show that syntaxin clusters are conserved, that NSF colocalizes with them, and characterize SNARE populations within and near these clusters using cryo-EM. Supercomplexes of NSF, α-SNAP, and either a syntaxin tetramer or two binary complexes of syntaxin—SNAP-25 reveal atomic details of SNARE processing and show how sequential ATP hydrolysis drives disassembly. These results suggest a functional role for syntaxin clusters as reservoirs and a corresponding role for NSF in syntaxin liberation and SNARE protein quality control preceding fusion.

40 # Introduction

41 The membrane-anchored SNARE (soluble N-ethylmaleimide-sensitive factor acceptor protein
42 receptor) proteins provide the energy to drive membrane fusion in various cellular contexts, such
43 as intracellular trafficking and exocytosis. One critical exocytic process is synaptic transmission,
44 in which a synaptic vesicle fuses with the presynaptic plasma membrane in the active zone of a
45 neuron to release neurotransmitter into the synaptic cleft in response to the arrival of Ca^{2+} in the
46 presynapse. While many proteins precisely act in concert to ensure synchronized and efficient
47 Ca^{2+}-triggered fusion[1–5], this process is fundamentally mediated by the "zippering" of four
48 SNARE motifs typically contributed by three to four SNARE proteins in the neuronal context—
49 syntaxin-1a and SNAP-25 on the target plasma membrane (*t*-SNAREs), and synaptobrevin-2 on
50 the vesicle (*v*-SNARE)—which come together to form a highly stable parallel four-helix bundle
51 during Ca^{2+}-triggered membrane fusion. This *cis*-SNARE complex must then be disassembled in
52 an ATP-dependent manner by the AAA+ protein NSF in concert with the adaptor SNAP
53 proteins[6,7].

54 While the molecular mechanisms of this core fusion cycle and the accessory proteins required to
55 ensure Ca^{2+}-dependent neurotransmitter release have been extensively studied[4], the organization
56 of the various components in the context of the crowded cellular milieu remains uncertain.
57 Numerous studies suggest nanoscale organization within the presynaptic active zone, where
58 proteins and lipids[8–11] such as cholesterol and PIP_2 colocalize or even phase separate into discrete
59 clusters with implications for organization within the active zone and even across the synapse[12].

60 The SNARE protein syntaxin shows such organization. Syntaxin is conserved from yeast to
61 mammals[13,14]; a short C-terminal transmembrane domain, a SNARE domain, and a C-terminal

62 Habc domain characterize it[15,16]. In the neuronal context, the majority (~ 67%) of syntaxin
63 molecules form nanodomains of non-uniform density[17,18], often near the active zone[8,17–21], and
64 these nanodomains frequently overlap with other essential active zone proteins and even docked
65 granules[19,20,22–25]. Morphologically, they are dense, around 50–60 nm in diameter, and harbor as
66 many as 70 syntaxin molecules each[17–19,22,26]. Increased presynaptic activity drives a decrease in
67 syntaxin cluster size[27]. These clusters depend on the syntaxin SNARE domain (H3), which
68 drives oligomerization[28].

69 Despite extensive study, the functional purpose of these clusters has remained unclear. Moreover,
70 NSF, α-SNAP, and syntaxin appear to interact *in vitro*[29], and α-SNAP associates with liposomes
71 presenting reconstituted full-length syntaxin[30]. Binary (syntaxin—SNAP-25) complexes of
72 different stoichiometries may also form [31–37], and NSF disassembles these complexes *in*
73 *vitro*[31,38–40]. Furthermore, continuous ATP hydrolysis by NSF on plasma-membrane mimicking
74 vesicles with reconstituted syntaxin and SNAP-25 produces a primed state for the most efficient
75 and synchronous synaptic vesicle fusion[3]. These observations support a critical role for NSF not
76 only in recycling SNARE proteins following fusion, but also in regulating the pool of fusogenic
77 syntaxin available to enter the vesicle fusion cycle.

78 Here, we show that spatially organized homo- or hetero-oligomers of syntaxin serve as
79 conserved molecular protein stores, and that NSF disassembles syntaxin nanodomains while
80 acting as a quality control factor to disassemble off-pathway binary complexes of syntaxin and
81 SNAP-25—a prerequisite for synaptic vesicle priming and fusion. We also describe the
82 molecular mechanism of disassembly and present a sequential ATP hydrolysis mechanism by
83 which NSF couples γ-phosphate release to SNARE substrate remodeling, with broad
84 implications for the AAA+ protein family.

85 # Results

86 ## Syntaxin nanodomains are conserved hotspots of NSF activity

87 First, we hypothesized that NSF is enriched at syntaxin clusters in the active zone, where it must
88 act to liberate fusogenic syntaxin molecules. To test this, we monitored the colocalization of
89 syntaxin and NSF in PC12 cells, a model system for neuronal secretion, using structured
90 illumination microscopy (SIM). All cells were transfected with GFP-syntaxin and as well NSF
91 with either a short C-terminal linker followed by mScarlet-I (NSF-mScarlet-I; Fig. 1A), a mutant
92 form of NSF (NSF(ΔN)-mScarlet-I; Fig. 1B,), or mScarlet-I alone (Fig. 1C). NSF-mScarlet-I is
93 hexameric and, together with α-SNAP, retains the capacity to bind and disassemble the ternary
94 SNARE complex (Fig. S1E). Clear, punctate co-clustering between NSF and syntaxin is visually
95 apparent upon inspection of the micrographs (Fig. 1A–C); Pearson's colocalization coefficient
96 (PCC) was calculated between the green and red channels to quantitate this (Fig. 1D, Methods).
97 Cells transfected with both GFP-syntaxin and NSF-mScarlet-I showed significant and
98 reproducible GFP-syntaxin-NSF-mScarlet-I colocalization (Fig. 1A, PCC = 60% ± 2%; $p <$
99 0.001 vs. mScarlet-I only;), suggesting an interaction between NSF and syntaxin molecules
100 within the nanodomains. As a control, mScarlet-I alone did not colocalize with syntaxin, showing
101 a nearly three-fold reduction in colocalization (Fig 1C; PCC = 22% ± 2%). To verify that
102 colocalization is consistent with the binding mode of NSF, in which NSF N-domains engage
103 multiple α-SNAPs, which in turn coat the SNARE complex[6,40,41], we examined colocalization of
104 GFP-syntaxin with a mutant form of NSF with the N-domain required for α-SNAP binding—and
105 thus SNARE complex binding—removed (NSF(ΔN)-mScarlet-I)[42]. As expected, this reduced
106 colocalization to a level nearly indistinguishable from the mScarlet-I control (Fig. 1B, PCC =
107 28% ± 3%; $p = 0.1776$ vs. mScarlet-I only). Two previously characterized[43] point mutations to

108 the D2 domain also disrupted colocalization between syntaxin and NSF (Fig. S1A–B). These
109 colocalization studies suggest that NSF associates with some multimeric species involving
110 syntaxin molecules *in vivo.* While these results showed clustering of syntaxin in the context of
111 synaptic transmission, we found that clustering also occurs in the case of the conserved syntaxin
112 homolog in yeast, Sso1p, as well (Fig 1F). During cell division, the mother cell transfers cargo to
113 the budding daughter cell via secretory vesicles; Sso1p clusters are enriched in the budding cell
114 in areas undergoing active fusion.

115 Discovery of a syntaxin tetramer complex with NSF—α-SNAP

116 To gain insight into the contents of the syntaxin nanodomains as well as the molecular basis of
117 the interaction between NSF and syntaxin, we purified the complex consisting of NSF, α-SNAP,
118 and soluble syntaxin (residues 2–253, transmembrane region omitted) by mixing the individual
119 purified proteins and performing size exclusion chromatography (SEC), Fig. S2A). We then
120 performed cryo-EM single-particle analysis (SPA) of this complex. Following 3D classification,
121 5% of the particles formed a class with an overall resolution of 3.75 Å, revealing a complex
122 (referred to as sx20S) between hexameric NSF, four α-SNAP molecules, and a parallel four-helix
123 bundle of syntaxin H3 SNARE domains (sx20S; Fig. 2A, Fig. S3, Tables S1–2). The remaining
124 particles showed no evidence of SNARE substrate. The existence of a syntaxin tetramer is
125 consistent with crosslinking mass spectrometry analysis of purified soluble syntaxin[36]. The
126 sx20S complex further supports the notion that NSF and α-SNAP recognize parallel, four-helix
127 SNARE complexes of variable composition[6,7].

128 Similar to structures of hexameric NSF and α-SNAP bound to the neuronal ternary SNARE
129 complex (referred to as 20S complex) under non-hydrolyzing conditions[6,41], the sx20S complex

130 forms a three-tiered architecture (Fig. 2A). NSF comprises three structured domains connected
131 by flexible linkers—the adaptor N-domain followed by the D1 and D2 AAA+ domains. Six NSF
132 protomers come together to form the active form of the enzyme, a homo-hexamer. In the top tier,
133 or spire, the NSF hexamer's multiple N domains bind four α-SNAP molecules and a tetramer of
134 syntaxin H3 SNARE domains. This spire structure positions the N-terminal end of the syntaxin
135 tetramer near the pore of the hexameric D1 ATPase ring of NSF; this middle tier is responsible
136 for ATP hydrolysis and SNARE complex disassembly. The bottom tier consists of the inactive
137 NSF D2 ATPase ring responsible for the oligomerization of the complex.

138 The spire structure is dynamic and rocks about relative to the D1 pore, but three of the six N
139 domains are relatively well-ordered and engaged with the α-SNAP—syntaxin sub-complex. The
140 D1 ring is asymmetric and split; protomers A–F are defined from the bottom of the split to the
141 top. All six D1 domains are ordered and engage the N-terminal linker preceding the H3 domain
142 of one of the four syntaxin molecules via conserved pore loops, which position Y294 such that it
143 intercalates between every other syntaxin substrate side chain passing through the pore (Fig. 2B).
144 The nucleotide states of the NSF ATPase domains are consistent with a pre-hydrolysis
145 conformation; D1 protomer A is ADP bound, while D1 protomers B–F are ATP bound with no
146 evidence for divalent cation as expected (Table S2). All D2 protomers are ATP bound and lack
147 divalent cation.

148 While the spire in the complete sx20S complex reconstruction was ordered enough to distinguish
149 the various components, continuous disorder limited the local resolution of the spire
150 reconstruction. To overcome this, we performed signal subtraction to remove the D1 and D2
151 rings, followed by local alignment of the α-SNAP—syntaxin sub-complex structure alone (Fig.
152 S3, Methods). This approach improved the resolution of the reconstruction of the α-SNAP—

153 syntaxin sub-complex to 4.25 Å, revealing a parallel, four-helix bundle of syntaxin SNARE
154 motifs with a density of sufficient quality to assign characteristic side chains (Fig. 2C). All four
155 helices are aligned in the same register, with a unique hydrophobic layer (-3 layer) composed of
156 four F216 side chains present; remarkably, all fit within the core of the bundle (Fig. 2D, Fig.
157 S9A) and induce little overall deformation of the individual H3 domains (Fig. S9B-D, bottom
158 row). The parallel syntaxin tetramer bundle observed in our structure would allow membrane
159 incorporation of the C-terminal transmembrane domains of all four syntaxin molecules (Fig. 2A).

160 To determine whether NSF and α-SNAP act to disassemble the syntaxin tetramer, we devised an
161 *in vitro*, gel-based disassembly assay (Fig. 1E). Wild-type NSF, α-SNAP, and soluble syntaxin
162 (residues 2–253) were purified independently, mixed in the absence of Mg^{2+} (*i.e.*, non-
163 hydrolyzing conditions), and the complex of all three was purified. The subsequent addition of
164 Mg^{2+} to the purified complex resulted in a significant loss of α-SNAP—syntaxin following
165 filtration relative to the non-hydrolyzing control, consistent with the disassembly of the syntaxin
166 tetramer and concurrent disassociation of α-SNAP (Fig. 1E, 21 ± 1% loss; Fig. S1D).

167 Structure of a 2:1 syntaxin—SNAP-25 complex with NSF—α-SNAP

168 In addition to the syntaxin homo-tetramer, hetero-oligomers with SNAP-25 are expected to be
169 present near or even within syntaxin nanodomains. Indeed, SNAP-25 colocalizes with syntaxin
170 in neurons[19,22,24] and readily forms binary complexes with syntaxin *in vitro*[31–35,44,45]. Although
171 SNAP-25 is required for fusion, assembly of a fusogenic ternary *trans*-SNARE complex likely
172 proceeds first through a syntaxin—synaptobrevin intermediate templated by Munc18-1, also
173 colocalized to syntaxin clusters[24], and by Munc13-1[31,46,47]. Disassembly of the binary complex is
174 critical, as genetic deletion of NSF is lethal[48]. However, an NSF mutation that differentially

175 blocks ternary, but not binary, SNARE complex disassembly causes only intermediate
176 sensorineural defects[38]. Thus, NSF and α-SNAP must first disassemble binary complexes of
177 syntaxin and SNAP-25 to set the stage for the action of Munc18 and Munc13, ultimately
178 resulting in synchronous and efficient Ca^{2+}-triggered fusion[3,31,32,46].

179 To gain insight into the structural nature of binary complex formation and disassembly by NSF,
180 we prepared a complex of NSF, α-SNAP, and the binary *t*-SNARE complex (21bin20S)
181 composed of full-length soluble SNAP-25 and soluble syntaxin-1a (1–267) in the absence of
182 divalent cation (*i.e.*, non-hydrolyzing conditions) and performed single-particle cryo-EM (Tables
183 S1–2, Fig. S2B, Figs. S4–5). First, models of the NSF D1 and D2 domains with substrate bound
184 in the D1 pore were built into two high-resolution (2.88 Å, 2.92 Å) classes from a single dataset,
185 differing only in the state of F protomer engagement with substrate (Fig. S4). Next, the dataset
186 from which they were derived was combined with two additional datasets to enable the 3D
187 reconstruction of weakly populated states with ordered density for the α-SNAP—SNARE spire
188 (Fig. S5). Classes with evidence of NSF D1 domains engaging ordered α-SNAP—SNARE sub-
189 complexes were carried forward; eight 21bin20S models were built into reconstructions ranging
190 from 3.39–4.01 Å in resolution, differing mainly in the orientation of N domains and a sub-
191 complex of three α-SNAP molecules and four SNARE motifs relative to the D1 ATPase ring
192 (Fig. S10A). All classes revealed substrate-bound NSF without Mg^{2+} needed for ATP hydrolysis
193 and disassembly (Table S2), and share the same overall architecture, with a spire composed of
194 NSF N-domains and the α-SNAP—SNARE subcomplex on top, the NSF D1 ring in the middle
195 tier, and the NSF D2 ring forming the bottom tier (Fig. 3A). In all cases, the NSF D1 ATPase
196 ring engages SNARE substrate, with one syntaxin molecule bound to the D1 ring pore in most
197 structures (Fig. 3B, Table S2).

198 Like the sx20S complex, continuous variability of the α-SNAP—SNARE subcomplex was
199 present in the 21bin20S reconstructions. We again performed signal subtraction and local
200 alignment on α-SNAP—SNARE sub-complexes from all five classes with ordered spire
201 structures (Fig. S5; see Methods). This procedure produced a single α-SNAP—SNARE sub-
202 complex reconstruction with an overall resolution of 3.74 Å (Fig. 3C), sufficient to assign
203 characteristic side chains, identify the SNAREs forming the complex and their directionality
204 (Fig. 3D, Fig. S9A). A model composed of the ternary neuronal SNARE complex[49] (PDB ID
205 1N7S) with synaptobrevin removed was docked into the density, preserving a distinctive kink in
206 the peptide linker leading into the SN2 SNARE motif of SNAP-25. In place of synaptobrevin, a
207 second syntaxin molecule was placed to complete the four-helix bundle with little deviation from
208 its usual backbone configuration of the ternary complex (Fig. S9B). As such, the stoichiometry
209 of the syntaxin—SNAP-25 complex observed is 2:1, the dominant species in solution[33,36,44,45].
210 Sidechains comprising essential layers repack within the core of the complex (Fig. 3D) compared
211 to the ternary SNARE complex. For example, the ionic central layer (0 layer) is reorganized;
212 Arg56 of synaptobrevin is replaced with a second Gln226 from the additional syntaxin molecule,
213 which adopts an extended rotamer to mimic the arginine it replaces. The SNAP-25 linker, which
214 joins the two SNARE motifs, is largely disordered but blocks binding by a fourth α-SNAP
215 molecule, as observed for the neuronal SNARE complex[6].

216 Docking the 2:1 binary complex structure back into the seven individual 21bin20S
217 reconstructions reveals an apparent preference for syntaxin, with six of eight reconstructions
218 featuring the N-terminus of syntaxin H3 bound within the pore of the D1 ring (Fig. 3B). As in the
219 case of the 20S with ternary SNARE complex, this observation is consistent with previous work,
220 in which disassembly was not contingent on specific SNARE N-terminus identity[6,40]. Taken

221 together, we observe that the NSF D1 ring can bind to at least two different SNAREs, syntaxin,
222 and SNAP-25, in various configurations.

223 Structure of a 2:2 syntaxin—SNAP-25 complex with NSF—α-SNAP

224 To gain insight into the disassembly of the binary SNARE complex, we repeated the binary 20S
225 preparation but added Mg^{2+} and an ATP regeneration system[50] (*i.e.*, hydrolyzing conditions) to
226 the purified complex ~1 min before vitrification for single particle cryo-EM (Tables S1–2, Fig.
227 S2C, Fig. S6). The addition of the regeneration system more closely mimics the metabolic state
228 of the cell, and it allows multiple cycles of SNARE disassembly and reassembly to proceed as
229 observed under far more dilute conditions[32]. Following 3D classification, 41% of particles
230 formed a complete complex, all of which have ordered α-SNAP—SNARE spire density and
231 differ largely by spire pose (Fig. S10A). Interestingly, classes with poorly defined SNARE
232 substrate, as observed under the non-hydrolyzing condition, were no longer observed. The
233 remaining 59% of particles were SNARE-substrate free and grouped into three classes with split
234 D1 and D2 rings; presumably, this is a post-disassembly, substrate-released state, and it is not
235 observed under non-hydrolyzing conditions.

236 Substrate-bound reconstructions reveal a flattened D1 ring in closer proximity to the D2 ring and
237 a strikingly different α-SNAP—SNARE spire structure than observed in the 21bin20S complex
238 under non-hydrolyzing conditions (Fig. 4A, Fig. S11A). Again, syntaxin is bound within the pore
239 of the D1 ring (Fig. 4B, Table S2). We observed a nearly symmetric α-SNAP—SNARE
240 subcomplex comprising four α-SNAP molecules coating a four-helix bundle. Even without
241 further processing, this structure was recognizable as a 2:2 syntaxin—SNAP-25 sub-complex
242 formed by two syntaxin H3 SNARE domains and two SNAP-25 SN1 SNARE domains; this

243 binary 2:2 configuration was previously observed in crystal structures of syntaxin-1 H3 and
244 SNAP-25 SN1 domains[34] and was unexpected as we prepared the complex with full-length
245 proteins, implying that two independent SNAP-25 molecules contribute their SN1 SNARE
246 domains to this complex. Presumably, disassembly of the binary 2:1 complex (Fig. 3C) had
247 occurred and was followed by reassembly to form the 2:2 binary complex (Fig. 4C) before
248 vitrification.

249 To improve the resolution of the spire reconstruction, signal subtraction, and local alignment
250 were performed as before (Fig. S6). This approach improved the reconstruction of the spire
251 proteins to 4.22 Å, enabling docking of a crystal structure of the 2:2 syntaxin—SNAP-25 SN1
252 complex[34] into the density (Fig. 4C), which was of sufficient quality to assign characteristic side
253 chains, to identify the SNARE domains and their directionality (Fig. 4D, Fig. S9A). The 2:2
254 binary complex was fit back into the full reconstructions, enabling modeling of the full
255 22bin20S. Furthermore, we were able to reproduce this result by reconstituting the complex with
256 only the SNARE domains of syntaxin and SNAP-25 under non-hydrolyzing conditions
257 (min22bin20S, Fig. S7A–D), yielding the same spire configuration but to a higher resolution of
258 3.86 Å following local reconstruction (Fig. S7E, Fig. S9A). This reconstruction also reveals the
259 interface between an N-domain of NSF and an α-SNAP molecule in detail; the interface is
260 characterized by a core hydrophobic interaction surrounded by charge complementation (Fig.
261 S7F).

262 Insights into SNARE substrate engagement and processing by NSF

263 Collectively, we obtained many datasets with NSF, α-SNAP, and several SNARE substrates
264 under non-hydrolyzing and hydrolyzing conditions (Tables S1–2), presenting an opportunity to

265 investigate the molecular mechanism of SNARE substrate processing and chemomechanical
266 energy transduction in NSF. Together, the resulting high-resolution structures derived from the
267 different classes from these datasets capture the hydrolysis cycle of NSF and reveal important
268 details about its reaction coordinate (Fig. 5–6, Figs. S11–13, Table S2).

269 For datasets with particles collected under non-hydrolyzing conditions, NSF is found in two
270 general conformations, primarily differentiated by their F protomer state (Fig. 5A, left column).
271 Two high-resolution 21bin20S classes from the 2:1 binary SNARE complex dataset reveal large-
272 scale conformational displacement connected to D1 F promoter nucleotide state and SNARE
273 substrate engagement. The first class is ATP-bound and fully SNARE substrate-engaged, while
274 the second has a nucleotide-free and SNARE substrate-disengaged F protomer (Fig 5A, left, top,
275 and bottom, respectively; Fig. S4). The engagement of F at the top of the ring accompanies a
276 relaxation of A into the split. Otherwise, the classes are nearly identical; protomers B–E D1
277 domains also bind ATP, while protomer A, at the bottom of the D1 split, is ADP-bound in both
278 cases. Comparison of the two classes reveals limited differences outside of the protomers A and
279 F positions, as the change in protomer F position allows additional relaxation of protomer A into
280 the split.

281 In contrast to the non-hydrolyzing datasets, particles in the hydrolyzing dataset fall into two
282 categories—substrate-bound 22bin20S (Fig. 5A, middle column) or substrate-free NSF (post-
283 hydrolysis; Fig. 5A, right column), of which there are ten and three classes, respectively (Table
284 S2, Fig. S6). The particles show a population shift towards a flatter D1 ring that is closer to D2
285 relative to the non-hydrolyzing class, particularly in the case of the SNARE-substrate free classes
286 (Fig. S11). Most strikingly, no SNARE substrate-bound classes show an F protomer as fully
287 engaged as those in non-hydrolyzing classes; in all but one class, F is ADP bound, SNARE

288 substrate disengaged, and sits between engaged A and E protomers. However, a subclass with an
289 ATP-bound F protomer was found using a subdivision of a large class with 3D Variability
290 Analysis[51] (3DVA; Fig. S6, Fig. 12C–D) for which the interprotomer interface with the
291 neighboring D1 protomer E is nearly—but not completely—formed. Critically, the pore loop
292 approaches the substrate-engaged state found in the non-hydrolyzing classes; together, this
293 reveals a trajectory of protomer A dissociation, nucleotide release and rebinding, and, finally,
294 SNARE substrate rebinding (Fig. 5D). Furthermore, classes with ordered syntaxin substrate are
295 gripped by the tyrosine residues in the pore of the D1 ring around eight residues further into the
296 primary sequence under hydrolyzing conditions (Fig. S10B).

297 Sequential hydrolysis by NSF drives conformational cycling

298 As noted above, the nucleotide states of the D1 protomers help explain the pattern of engagement
299 with the SNARE substrate (Fig. 5A–C, Table S2). How does nucleotide hydrolysis drive this
300 process? Unlike the non-hydrolyzing 21bin20S reconstructions, hydrolyzing 22bin20S
301 reconstructions are only ATP-bound in protomer E, indicative of a sequential hydrolysis
302 mechanism (Fig. 5A, middle column). Except for the rebinding F protomer described above, all
303 other D1 protomers are ADP bound with variability in the presence of Mg^{2+} and inorganic
304 phosphate (P_i); in most cases, protomers C and D have ADP•P_i and Mg^{2+}, protomer B is ADP-
305 bound, and protomer A is typically ADP-bound only. Finally, substrate-free classes are always
306 ADP bound, even in protomer E; they are flat, have some N-domains packed between the D1 and
307 D2 rings, and are characterized by a split in both the D1 and D2 rings between protomers A and
308 F (Fig. 5A, right column); this is consistent with a SNARE substrate side-loading mechanism
309 proposed for the NSF ortholog in yeast, Sec18[52]. In both hydrolyzing and non-hydrolyzing
310 datasets, all D2 domains are ATP-bound, with Mg^{2+} present in the hydrolyzing condition.

311 Together, these classes represent key steps in the hydrolysis cycle, revealing the binding of Mg^{2+},
312 hydrolysis of ATP to ADP•P_i at protomer E, and subsequent P_i release down-ring; these states are
313 accompanied by conformational change in the Walker A, Walker B, and Sensor 1 active site
314 residues in *cis* and the arginine fingers of the down-ring protomer in *trans* (Fig. 5B), and are
315 connected in turn to larger scale conformational change within the D1 domain (Fig. 5C).
316 Critically, P_i release following hydrolysis leads to arginine finger disengagement (Fig. 5B, right
317 two panels) and subsequent relaxation and solvation of the interprotomer interface, enabling the
318 protomer A transition to protomer F and subsequent substrate rebinding.

319 What triggers hydrolysis at E, and what conformational changes follow? While hydrolysis could
320 proceed spontaneously, this would be inefficient in the absence of an ATP-bound protomer F up-
321 ring to capture accompanying substrate translocation. We hypothesized that some allosteric
322 mechanism must regulate this process. To identify such a mechanism in an unbiased manner, we
323 performed principal components analysis (PCA) of Cα coordinates of 132 D1 protomers across
324 all datasets followed by hierarchical density-based clustering (HDBSCAN) in high-dimensional
325 space, revealing the conformational cycling of the NSF D1 protomers in a low-dimensional
326 coordinate as well as a corresponding allosteric mechanism for modulating hydrolysis by
327 protomers E (Fig. 6; see also Methods).

328 Overall, we find protomers divided into five interpretable clusters connected to ATP hydrolysis,
329 P_i release, and protomer cycling at the D1 split during SNARE disengagement, nucleotide
330 rebinding, and SNARE reengagement (Fig. 6A). Here, we focus on the unique features of the
331 protomers E under hydrolyzing conditions in two dimensions of the 11-dimensional latent space,
332 where they cluster far from other protomers (Fig. 6A, transition 1). As noted above, protomers E
333 are the only ATP-Mg^{2+} bound D1 protomers under hydrolyzing conditions (Fig. 6B), and they are

334 uniquely characterized by an extreme large-small subdomain angle (Fig. 6C, Fig. S11).
335 Examination of PCA and clustering results reveal conformational states unique to these
336 protomers (Fig. 6E), notably a discrete Walker A (α_3) helix position ("down" state) relative to the
337 rest of the D1 large subdomain that uniquely positions the nucleotide near key catalytic residues
338 (N374, R388; Fig. S13), a unique conformation of a highly conserved[56] segment of the N-D1
339 linker connected to N-domain engagement ("up A" state), and the absence of a fully engaged
340 "latch loop" (residues 457–467) contributed by the up-ring protomer F in *trans* ("intermediate A"
341 state; Fig. S12A). All three of these features appear structurally coupled (Fig. S12B) and
342 comprise an allosteric integration mechanism by which the position of nucleotide in the active
343 site is modulated at a distance by both N-domain engagement to SNARE substrate via the N-D1
344 linker conformation and by the presence of an up-ring protomer F via latch loop engagement.

345 To test the importance of the latch loop interaction in *trans*, a mutant form of NSF was generated
346 in which a portion of the latch loop (residues 460–466) is replaced with a short glycine-serine
347 linker (SGS). An NSF activity assay based on fluorescence dequenching (see Methods) shows a
348 highly significant, ~72% reduction in the rate of SNARE complex disassembly ($p = 0.0005$; Fig.
349 6D). On the other hand, the functional importance of the N-D1 linker has already been
350 established. We note that a mutation to NSF in the most conserved region N-D1 linker, I209N,
351 has a direct behavioral effect in zebrafish; NSF(I209N) is defective in the disassembly of ternary
352 SNARE complexes but not binary SNARE complexes, explaining this phenotype[38,56]. This
353 isoleucine side chain directly contacts the engaged latch loop and is adjacent to S207, a putative
354 phosphorylation site[53], raising the possibility of post-translational modification in regulating NSF
355 activity. Together, these observations support an allosteric mechanism critical in both effecting
356 and modulating NSF function.

357 # Discussion

358 Our observation of NSF colocalization to syntaxin clusters *in vivo*, coupled with direct structural
359 evidence of disassembly of both syntaxin tetramers and syntaxin—SNAP-25 complexes,
360 explains a previously overlooked but essential aspect of the synaptic vesicle fusion cycle, with
361 broad implications for membrane trafficking (Fig. 7A). While NSF is well known for its role in
362 ternary *trans*-SNARE complex disassembly following fusion, this work, combined with
363 functional studies[3,31,32,46], also establishes NSF as a critical factor for synaptic vesicle priming
364 before fusion. NSF is enriched at and near syntaxin clusters, which are, in turn, found at the
365 presynapse. The observation here of a parallel, four-helix syntaxin-1a bundle suggests that these
366 clusters must be structured, at least in part, and that NSF and α-SNAP act to disassemble the
367 syntaxin tetramers on the perimeter of a given cluster, increasing syntaxin mobility at the
368 synapse[27]. Individual syntaxin molecules liberated from clusters by NSF can then be captured by
369 the SM protein Munc18 and ultimately be used to assemble fusogenic *trans*-SNARE complexes.

370 However, a high local concentration of SNAP-25 is present near the syntaxin clusters as well, so
371 free syntaxin may also enter a non-productive binary SNARE complex with SNAP-25 with a
372 stoichiometry dependent upon local concentrations and configurations of either protein. In this
373 work, we observe binary complexes with two stoichiometries—2:1 and 2:2 binary complexes of
374 syntaxin and SNAP-25, with the latter re-forming following NSF-mediated disassembly of the
375 former under hydrolyzing conditions. The 2:1 configuration dominates in the non-hydrolyzing
376 condition—and in other *in vitro* studies[33,45]—but is derived from co-expressed proteins that were
377 extensively purified without NSF action. The 2:2 configuration is only found following NSF-
378 mediated disassembly of the 2:1 configuration. This effect may be due to the dissociation of the
379 SNAP-25 SN1 and SN2 domains during disassembly by NSF, increasing the likelihood of

380 binding to other SN1 domains in *trans*. The structural plasticity of the SNARE complexes is also
381 of note; taken together, the repeated observation of a twisted, parallel, four-helix bundle with
382 minimal backbone distortion (Fig S9B) emphasizes the functional conservation latent in the
383 SNARE domain sequences studied thus far, as well as the importance of additional SNARE
384 protein accessory domains in differentiating SNARE protein function[52].

385 Regardless, NSF and α-SNAP must thus constantly act to disassemble both syntaxin tetramers
386 and binary SNARE complexes to maintain a fusogenic population of *t*-SNAREs[3], which
387 ultimately enter the *trans*-SNARE complex with the *v*-SNARE synaptobrevin-2 and set the stage
388 for Ca^{2+}-triggered fusion in cooperation with synaptotagmin and complexin[54,55]. Indeed, the
389 energy released by SNARE protein zippering during vesicle fusion should be related to the
390 hydrolysis of ATP by NSF, which effectively maintains them in a high-energy state. Thus,
391 syntaxin nanodomains could effectively act as high-density storage sites for syntaxin, and NSF
392 could tap these stores under periods of high-frequency vesicle release. Modulation of NSF
393 activity by post-translational modification could thus be one way to regulate this process[38].
394 Finally, given the observation of clustered Sso1p in yeast, and the high degree of structural and
395 functional conservation between NSF and Sec18[52], this seems likely to be a conserved
396 organizing principle across fusion contexts.

397 At the atomic level, how does NSF accomplish the energy transfer needed to disassemble various
398 SNARE complexes? The structural details of the hydrolysis cycle (Fig. 5) suggest sequential
399 hydrolysis by the six D1 ATPase domains of NSF. Hydrolysis drives conformational change,
400 which is coupled to the application of force to one member of the SNARE complex, destabilizing
401 it and promoting disassembly (Fig. 7B, Movie S1). Rather than relying on a non-physiological
402 nucleotide state promoted by chelation of divalent cations or non-hydrolyzable nucleotide

403 analogs (*e.g.*, ATPγS), we established a reaction condition more closely approximating cellular
404 metabolism by using a physiological ATP regeneration system. Critically, hydrolysis proceeds
405 sequentially around the asymmetric NSF D1 ring, occurring near the "top" of the ring at
406 protomer E. Down-ring protomers reveal evidence for a transient post-hydrolysis reaction state
407 in which ADP•P_i is generally observed before P_i release from protomers C or B and an associated
408 disruption and solvation of the interprotomer interface. This mechanism is likely conserved in
409 other members of the AAA+ family, such as p97 (Supplemental Discussion).

410 Furthermore, the continuous transition from protomer A at the bottom of the ring to protomer F
411 at the top follows ADP release and ATP rebinding (Fig. 7B, Movie S1). This cycling appears
412 coupled to the triggering of hydrolysis at protomer E in a process allosterically mediated by
413 several key structural elements. Protomers E in the hydrolyzing condition position ATP in the
414 active site via a unique pre-hydrolysis conformation of the Walker A helix. Presumably, full
415 protomer F rebinding triggers hydrolysis, likely driven by an allosteric shift associated with full
416 latch engagement with the N-D1 linker region and further formation of the interprotomer
417 interface (Fig. 6, Fig. S12).

418 Protomer F rebinding is also connected to the mechanism by which engagement of the SNARE
419 substrate is maintained during processing. In the absence of a completely protomer F-rebound
420 state in the hydrolyzing condition, however, we cannot distinguish between SNARE substrate
421 rebinding before or after protomer E hydrolysis; the former case (ATP in fully rebound F and E)
422 represents a classical "hand-over-hand" mechanism, while the latter case (ATP in fully rebound
423 F, ATP ADP•Pi in E), a ratchet mechanism in which F re-engages substrate during or
424 immediately following a translocation event driven by protomer E hydrolysis, locking in any
425 substrate translocation that took place[57]. Given the highly flattened D1 ring state of the SNARE-

426 substrate free classes with ADP•Pi in protomers E (Fig. S11), the latter case is perhaps more
427 likely; flattening upon hydrolysis at protomer E could exert a pulling force on the substrate, and
428 translocation would then effectively take place with substrate engagement by a new protomer F
429 and release of the old protomer A.

430 Together, our findings expand the role of NSF in the membrane fusion cycle while further
431 demonstrating its contribution as a model system for understanding energy transduction and
432 protein remodeling in AAA+ proteins. NSF acts as a mobile engine of the presynapse—working
433 together with the SNAP adaptor proteins to convert the chemical energy latent in ATP into the
434 physical work needed to organize, maintain, and drive synaptic function through disassembly of
435 a variety of SNARE proteins.

436 Acknowledgments

437 We thank Richard Held, Jeremy Leitz, Rama Ranganathan, Subu Subramanian, Benjamin White,
438 Susan Wu, and Minglei Zhao for stimulating discussions; E. Montabana and C. Zhang for
439 assistance with the electron microscopy data collection at the Stanford University cEMc; and
440 Paul D. Adams, Pavel Afonine, and Nigel Moriarty for assistance with PHENIX refinement.
441 Funding was provided by the US National Institutes of Health (NIH; RO1MH63105 to A.T.B.)
442 and the Helen Hay Whitney Foundation/HHMI (to K.I.W.). Molecular graphics and analyses
443 performed with *UCSF ChimeraX*, developed by the Resource for Biocomputing, Visualization,
444 and Informatics at the University of California, San Francisco, with support from National
445 Institutes of Health R01-GM129325 and the Office of Cyber Infrastructure and Computational
446 Biology, National Institute of Allergy and Infectious Diseases. This article is subject to HHMI's
447 Open Access to Publications policy. HHMI laboratory heads have previously granted a non-

exclusive CC BY 4.0 license to the public and a sublicensable license to HHMI in their research articles. Pursuant to those licenses, the author-accepted manuscript of this article can be made freely available under a CC BY 4.0 license immediately upon publication.

Author contributions

K.I.W. and A.T.B. developed the research plan and experimental strategy. K.Q. and J.D. performed the cellular imaging experiments in PC12 cells and analyzed the data. Y.A.K. and A.B. performed the cellular imaging experiments in yeast and analyzed the data. K.I.W., Y.A.K. S.C., L.E., and R.P. purified all proteins. K.I.W., S.C., and Y.A.K. performed the disassembly experiments. K.I.W. performed the cryo-EM experiments and analyzed the data. K.I.W. and A.T.B. wrote the manuscript with input from the other authors.

Declaration of interests

All authors declare no competing interests.

Supplemental information

Associated Supplemental information file: Supplemental Discussion, Supplemental Figures 1–13 Supplemental Tables 1–2.

Supplemental Movie 1

Figures

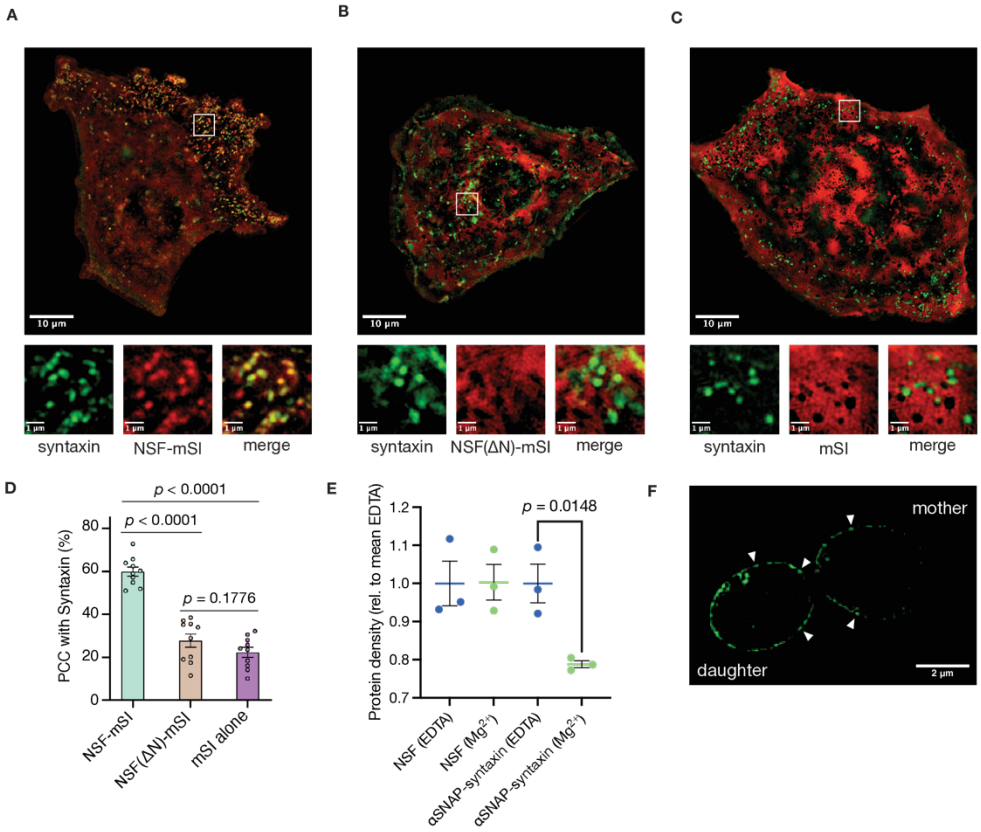

Figure 1 | NSF colocalizes to syntaxin nanodomains in an N-domain dependent manner and disassembles syntaxin oligomers

The interaction between NSF and syntaxin nanodomains in living cells. NSF-mScarlet-I and syntaxin-GFP were transfected into PC12 cells, and their conjugated fluorescent proteins were observed by SIM. Their interaction was assessed by measuring Pearson's colocalization coefficient (PCC) between the channels using *ImageJ*. Clustering of the syntaxin homolog Sso1p also occurs in yeast.

A. Colocalization between syntaxin-GFP nanodomains and wild-type NSF-mScarlet-I. NSF often forms punctate clusters that overlap with syntaxin (PCC = 60% ± 2%, mean ± SEM).

475 **B.** Colocalization between syntaxin-GFP nanodomains and NSF(ΔN)-mScarlet-I, in which the
476 N-domain of NSF that mediates the interaction with the α-SNAP—SNARE subcomplex has
477 been removed. Disruption of this interaction is evident and quantifiably reduces NSF
478 colocalization to syntaxin nanodomains (PCC = 28% ± 3%, mean ± SEM).

479 **C.** Control showing colocalization between syntaxin-GFP and mScarlet-I alone. No specific
480 interaction between these proteins is apparent (PCC = 22% ± 2%, mean ± SEM).

481 **D.** Comparison of wild-type NSF-mScarlet-I, NSF(ΔN)-mScarlet-I, and mScarlet-I clustering to
482 syntaxin-GFP nanodomains (M ± SEM, $n = 10$). Statistical significance was established by two-
483 tailed Student's *t*-tests, with $p < 0.05$ considered indicative of statistical significance.
484 Colocalization between wild-type NSF-mScarlet-I and syntaxin-GFP is significantly different
485 from both colocalization between NSF(ΔN)-mScarlet-I and syntaxin-GFP and colocalization
486 between mScarlet-I and syntaxin-GFP ($p < 0.0001$). Colocalization between NSF(ΔN)-mScarlet-
487 I and syntaxin-GFP and colocalization between mScarlet-I and syntaxin-GFP was not
488 significantly different ($p = 0.1776$).

489 **E.** NSF and α-SNAP disassemble oligomeric syntaxin as assessed by a gel-based de-enrichment
490 assay. sx20S was purified and split into two pools. EDTA was added to the first pool as a non-
491 hydrolyzing control, while Mg^{2+} was added to the second to initiate syntaxin complex
492 disassembly. Each pool was then concentrated using a 100,000 MWCO filtration device,
493 retaining 20S complex or α-SNAP—syntaxin subcomplex but allowing individual syntaxin and
494 α-SNAP molecules to pass, de-enriching them. Under hydrolyzing conditions, α-SNAP and
495 syntaxin were significantly de-enriched by around 21 ± 1% ($p = 0.0148$), consistent with the
496 disassembly of oligomeric syntaxin by NSF.

497 **F.** Sso1p forms dense clusters in the yeast plasma membrane during cell division (white

498 triangles). Sso1p-GFP was expressed in *S. cerevisiae* and imaged by SIM. Sso1p clusters were

499 enriched in the budding daughter cell (left); discrete clusters typically approached sizes near the

500 Nyquist limit of 160 nm (Fig S1C).

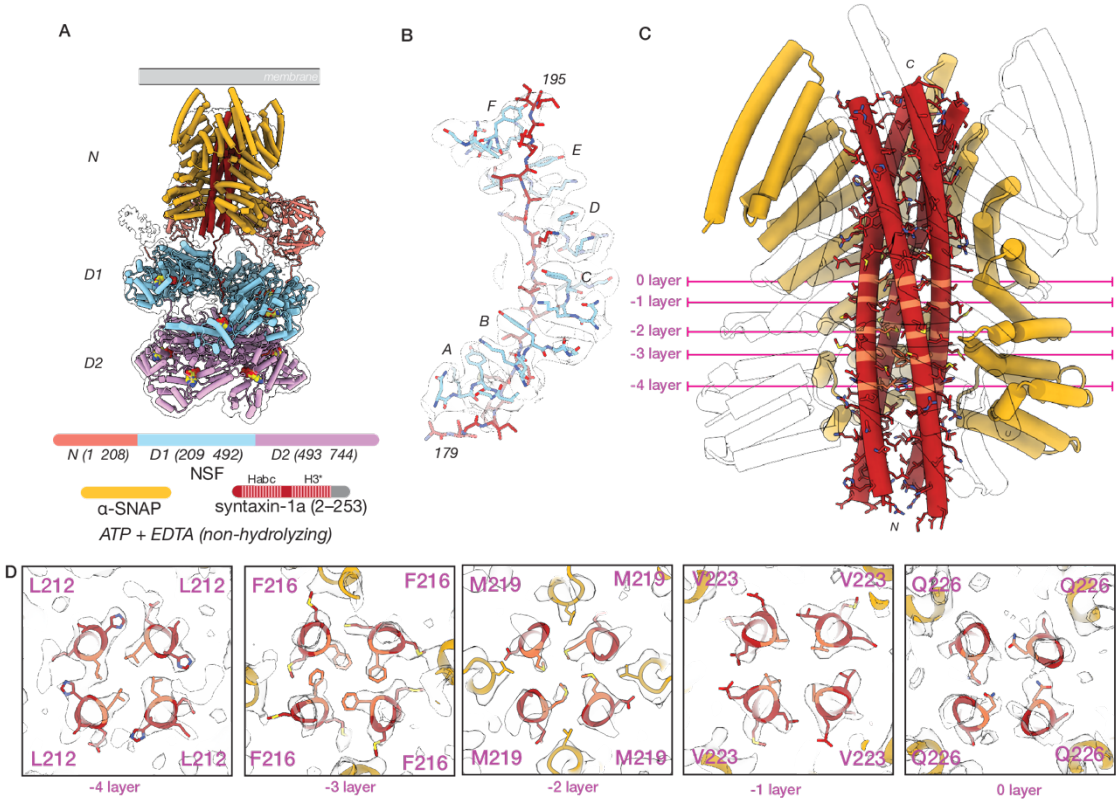

501

502 **Figure 2 | NSF and α-SNAP engage a tetrameric SNARE complex composed of four**
503 **syntaxin H3 domains**

504 The structures of the sx20S (class #1, 3.75 Å) and the α-SNAP—syntaxin tetramer subcomplex

505 (class #2, 4.07 Å).

506 **A.** Hexameric NSF engages the α-SNAP—syntaxin tetramer subcomplex via its N-domains

507 (salmon), several of which engage four α-SNAP molecules (gold) surrounding the soluble,

508 tetrameric syntaxin H3 complex (dark red) within the catalytic D1 ring of NSF (light blue). The

509 structural D2 ring of NSF (purple) does not engage the SNARE substrate. A hypothetical

510 membrane is illustrated in grey. For the SNARE proteins, domains visible in the reconstruction
511 of the SNARE complex are indicated with an asterisk; the syntaxin Habc domains were not
512 observed.

513 **B.** NSF engages one of the four syntaxin molecules in the tetramer via a series of pore loop
514 interactions; a tyrosine side chain (Y294) on each of the six protomers intercalates in between
515 every other side chain of a portion of syntaxin N-terminal to its H3 domain. The corresponding
516 sharpened map is contoured at 4 σ.

517 **C.** The α-SNAP—syntaxin tetramer subcomplex model, with two of the four α-SNAP models
518 hidden for clarity. The syntaxin H3 SNARE complex forms a twisted, parallel α-helical bundle
519 with a series of key SNARE complex layers preserved. See Fig. S9 for additional detail.

520 **D.** Slices through the α-SNAP—syntaxin tetramer subcomplex model and sharpened map at the -
521 4–0 layers, with key residues lightened for emphasis. Each layer is characterized by nearly planar
522 interactions between four identical side chains within the helical bundle. The primary
523 interactions between α-SNAP and the syntaxin H3 complex are observed near the -2 and -3
524 layers, where several functionally essential[58] α-SNAP side chains (L197, Y200) are positioned by
525 a loop that buries them within the groove of the bundle. No symmetry was imposed during
526 reconstruction.

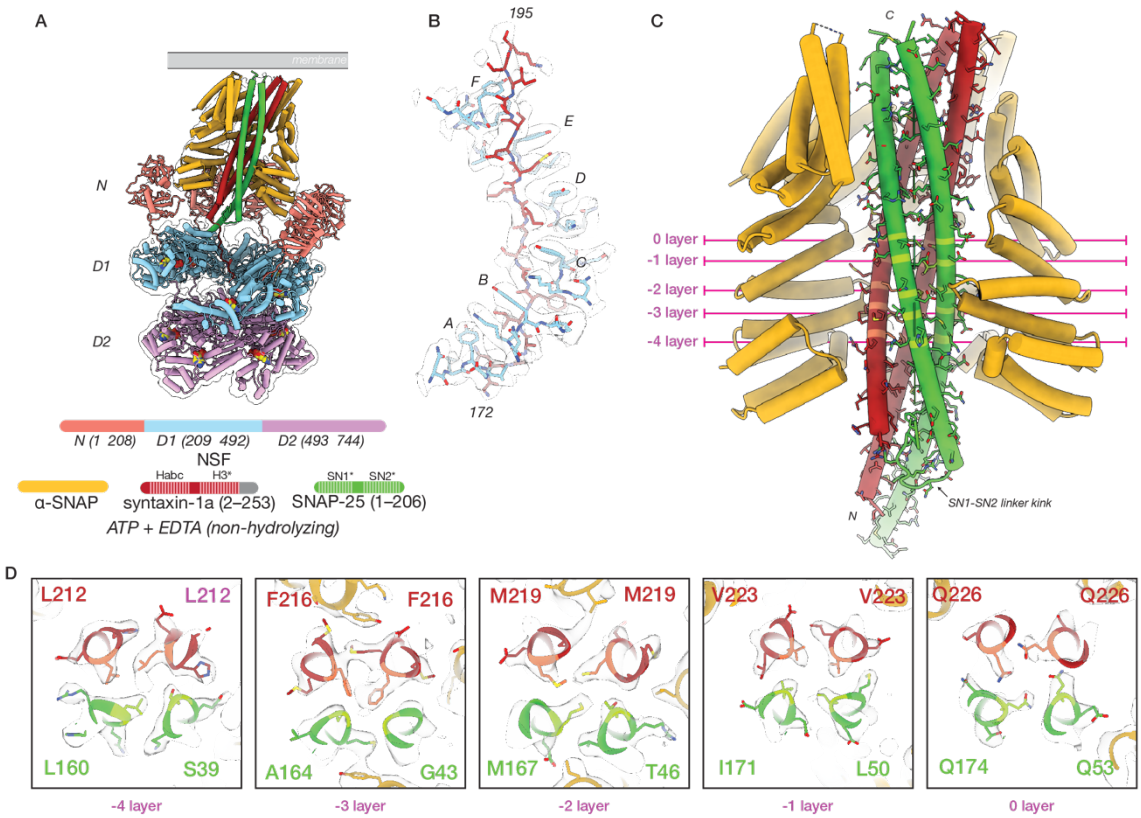

Figure 3 | NSF and α-SNAP engage a 2:1 binary SNARE complex of syntaxin H3 and SNAP-25 SN1 and SN2 SNARE domains under non-hydrolyzing conditions

A representative 21bin20S model (class #5, 3.39 Å) and the α-SNAP—2:1 binary SNARE subcomplex model (class #13, 3.74 Å).

A. Hexameric NSF engages the α-SNAP—2:1 binary SNARE subcomplex via multiple N-domains (salmon), which engage three α-SNAP molecules (gold) surrounding the 2:1 binary SNARE complex composed of two syntaxin H3 domains (dark red) and the SN1 and SN2 SNARE domains of a single SNAP-25 molecule (green). Part of the linker N-terminal to one of the syntaxin H3 domains is found within the catalytic D1 ring of NSF (light blue). The structural D2 ring of NSF (purple) does not engage the substrate. A hypothetical membrane is illustrated in grey. For the SNARE proteins, domains visible in the reconstruction of the SNARE complex are indicated with an asterisk.

540 **B.** NSF engages one of the two syntaxin molecules in the 2:1 binary SNARE complex via a
541 series of pore loop interactions involving Y294. A sharpened map is shown, contoured at 5 σ. Of
542 the eight 21bin20S classes with the 2:1 binary SNARE complex from the dataset collected under
543 non-hydrolyzing conditions, six have syntaxin molecules, and two have SNAP-25 molecules
544 bound to the pore of the D1 ring.

545 **C.** The α-SNAP—2:1 binary SNARE subcomplex model. Three α-SNAP molecules bind the 2:1
546 binary SNARE complex; a flexible linker between SNAP-25 SN1 and SN2 blocks access by a
547 fourth. The 2:1 binary SNARE complex forms a twisted, parallel α-helical bundle with a series
548 of characteristic SNARE complex layers preserved. This configuration also places the N-
549 terminal portion of the linker, which bears cysteines often palmitoylated *in vivo*, near the
550 membrane[59]. See Fig. S9 for additional detail.

551 **D.** Layer slices through the α-SNAP—2:1 binary SNARE subcomplex model and sharpened
552 map. Each layer is characterized by nearly planar interactions between four side chains within
553 the helical bundle. The primary interactions between α-SNAP and the syntaxin H3 complex are
554 found near the -2 and -3 layers, where several functionally essential[58] α-SNAP side chains (L197,
555 Y200) are positioned by a loop that buries them within the bundle groove.

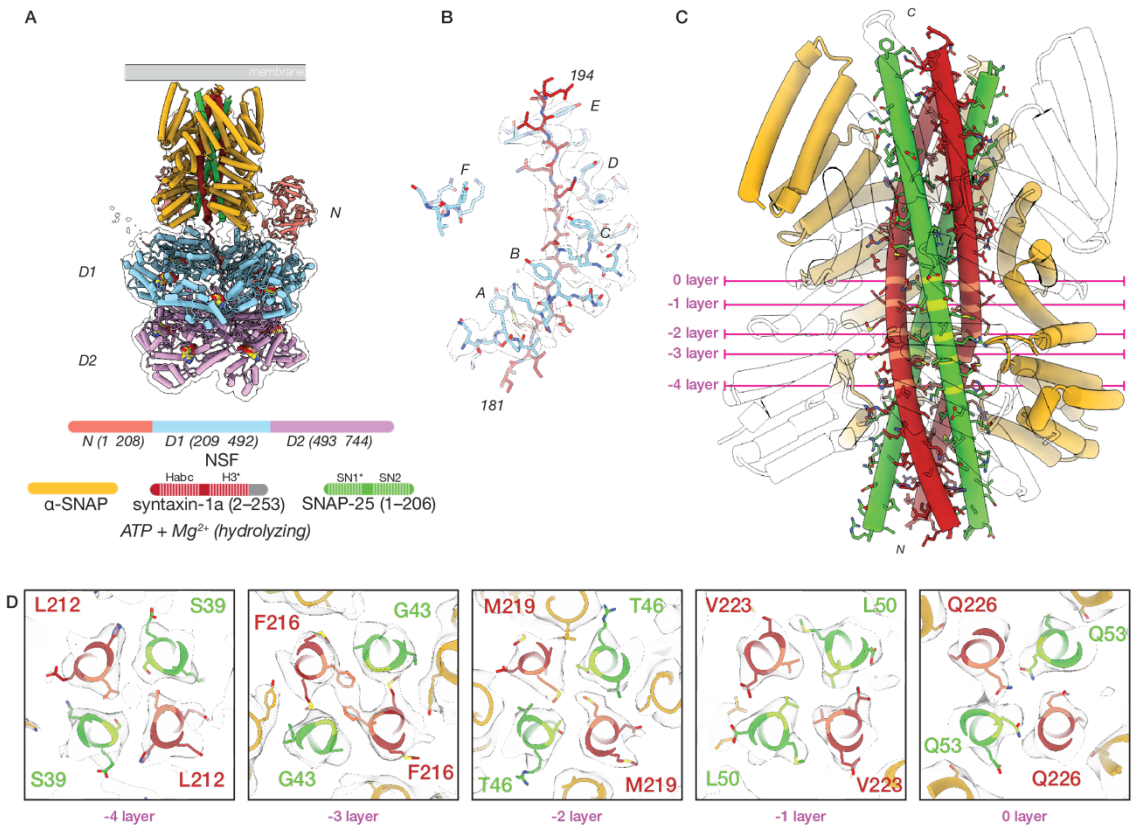

Figure 4 | NSF and α-SNAP engage a 2:2 binary SNARE complex of syntaxin H3 and SNAP-25 SN1 SNARE domains under hydrolyzing conditions

A representative 22bin20S model (class #19, 3.56 Å) and the α-SNAP—2:2 binary SNARE subcomplex model (class #23, 4.14 Å).

A. Hexameric NSF engages the α-SNAP—2:2 binary SNARE subcomplex via multiple N-domains (salmon), which engage three α-SNAP molecules (gold) surrounding the soluble, 2:2 binary SNARE complex composed of two syntaxin H3 domains (dark red) and two SNAP-25 SN1 domains contributed by two separate full-length SNAP-25 molecules (green). A portion of the linker N-terminal to one of the syntaxin H3 domains is observed within the catalytic D1 ring of NSF (light blue). The structural D2 ring of NSF (purple) does not contain density for a substrate. A hypothetical membrane is illustrated in grey. For the SNARE proteins, domains

568 visible in the reconstruction of the SNARE complex are indicated with an asterisk. See Fig. S9
569 for additional detail.

570 **B.** NSF engages one of the two syntaxin molecules in the 2:2 binary SNARE complex via a
571 series of pore loop interactions involving Y294. A sharpened map is shown, contoured at 6 σ. Of
572 the five 22bin20S classes with the 2:2 binary SNARE complex, all are found with syntaxin in the
573 D1 pore, while two are observed with the N-terminus of the SNAP-25 SN1 domain in the pore.

574 **C.** The α-SNAP—2:2 binary SNARE subcomplex model. Four α-SNAP molecules bind the 2:2
575 binary SNARE complex, with two SNAP-25 SN1 SNARE domains and two syntaxin H3
576 domains. This configuration would place two independent N-terminal portions of the SNAP-25
577 linker bearing cysteine sidechains often palmitoylated *in vivo* near the membrane[59].

578 **D.** Slices through the α-SNAP—syntaxin tetramer subcomplex at the -4–0 layers. Each layer is
579 characterized by nearly planar interactions between four side chains within the helical bundle.
580 The primary interactions between α-SNAP and the syntaxin H3 complex are found near the -2
581 and -3 layers, where several functionally essential[58] hydrophobic α-SNAP side chains, L197 and
582 Y200, are positioned by a loop that buries them within the bundle groove. Symmetry was not
583 enforced during local reconstruction. Note that the near-twofold symmetry of the bundle leaves
584 some sidechain densities poorly defined, likely resulting from the superposition of the syntaxin
585 and SNAP-25 residues in a given layer.

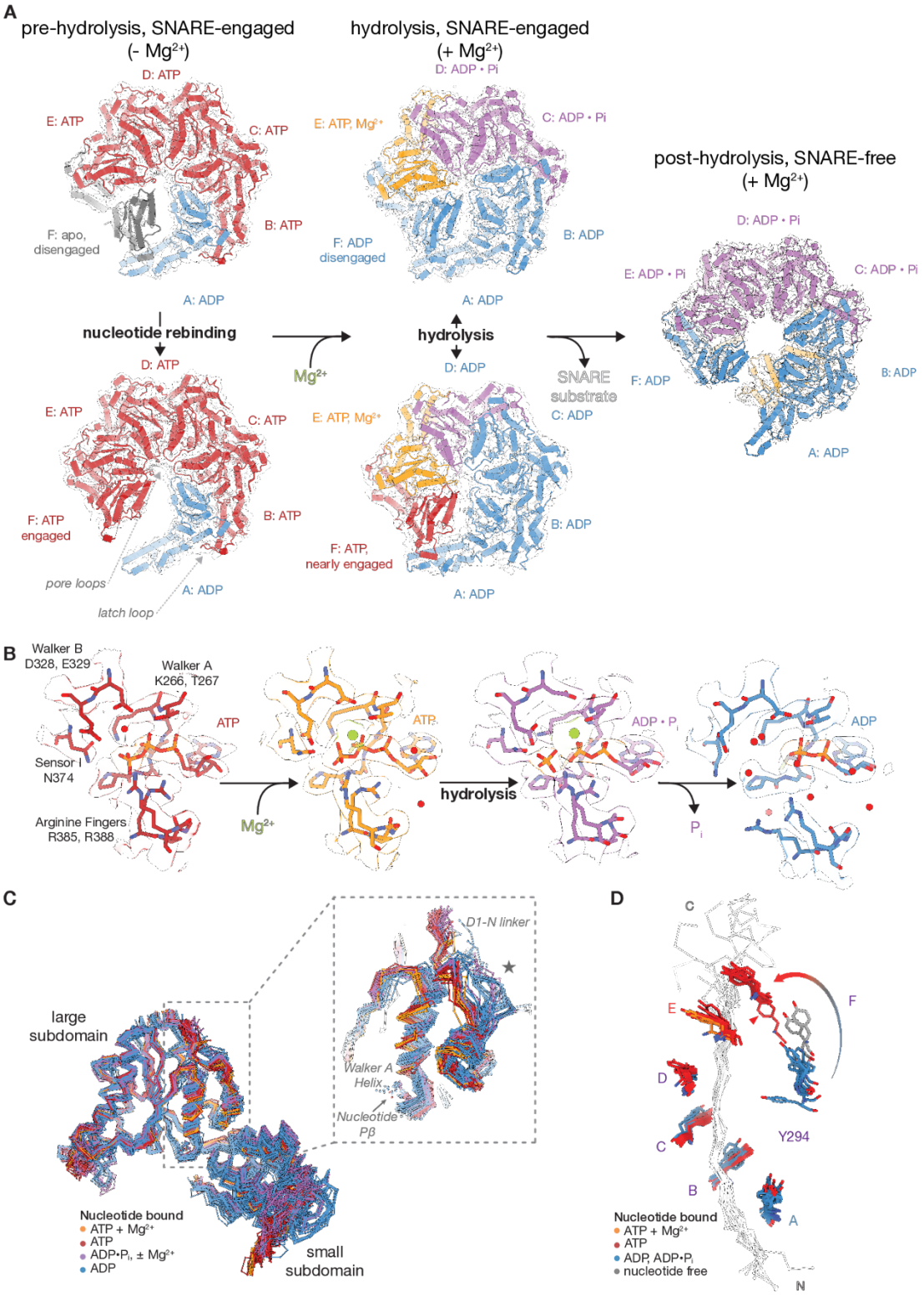

586

587 **Figure 5 | Comparison of NSF structures under non-hydrolyzing and hydrolyzing**
588 **conditions reveals interplay between sequential AAA+ hydrolysis and substrate rebinding**

589 **A.** Key conformational states of the NSF D1 ATPase ring. Two primary states dominate in the
590 absence of Mg^{2+} (left); the top class (#4) has a SNARE substrate disengaged, nucleotide-free
591 protomer F, while the bottom class (#3) has a fully SNARE substrate-engaged, ATP-bound F.
592 With the addition of Mg^{2+} (middle), E is ATP- and Mg^{2+}-bound. Protomers D, C, and
593 occasionally B retain P_i. and Mg^{2+}. All A protomers are ADP-bound. 3DVA-derived subclasses
594 reveal a coordinate for nucleotide exchange and protomer F engagement. The top subclass (#18)
595 has a substrate-disengaged, ADP-bound F. The bottom subclass (#17) has a nearly substrate-
596 engaged, ATP-bound F. Finally, substrate-free, post-hydrolysis classes such as #24 (right) show
597 an ATP-free D1 ring. For clarity, the spire, SNARE substrates, and the D2 ring are omitted in the
598 figures. See Tables S1–2 for more information on specific classes.

599 **B.** Atomic details of nucleotide hydrolysis. The P-loop binds nucleotide. Arginine fingers R385
600 and R388 from the down-ring protomer coordinate nucleotide phosphates. Without Mg^{2+}, a water
601 molecule sits between the nucleotide phosphates and Walker B residue side chains of D328 and
602 E329. Sensor 1 residue N374 is oriented towards the ɣ-phosphate of ATP. In the hydrolyzing
603 condition, Mg^{2+} appears in the active site, tightly coordinated by the β- and ɣ-phosphate moieties
604 of ATP and the side chain of Walker A motif T267. Following hydrolysis, ADP, P_i, and Mg^{2+}
605 remain; the side chains of Walker B residue E329 and Sensor 1 residue N374 tightly coordinate
606 the P_i as it disassociates. Subsequent P_i release down-ring leads to arginine finger disassociation,
607 disrupting the interprotomer interface. Active sites shown are derived (from left to right) from
608 D1 class protomers #4-E, #16-E, #16-D, and #16-B.

609 **C.** Alignment of 130 D1 protomers from 23 models derived from all four datasets. Structural
610 alignment was performed on the D1 large subdomains. Only Cα atoms of nucleotide-bound
611 protomers and corresponding Pβ atoms are shown for clarity. The inset (right) shows a key

612 region of the protein that shows changes in the N-D1 linker and N-terminus of the D1 domain
613 and the Walker A helix. The presence of the latch loop contributed by the up-ring protomer also
614 influences the conformational state of this region. In contrast, the loop is omitted for clarity, and
615 the binding location is indicated with a star.

616 **D.** Alignment of tyrosine residues in the pore of the D1 ring of substrate-bound models reveals
617 protomer F as the site of nucleotide exchange and substrate re-engagement. ADP-bound F is
618 disengaged from the substrate (blue). The release of ADP (nucleotide-free, grey) and ATP-
619 binding (red) are accompanied by a continuous transition to substrate engagement. The lowest
620 tyrosine corresponding to an ATP-bound F shown (red triangle) is from the 3DVA-derived model
621 shown in **A** (middle column, bottom).

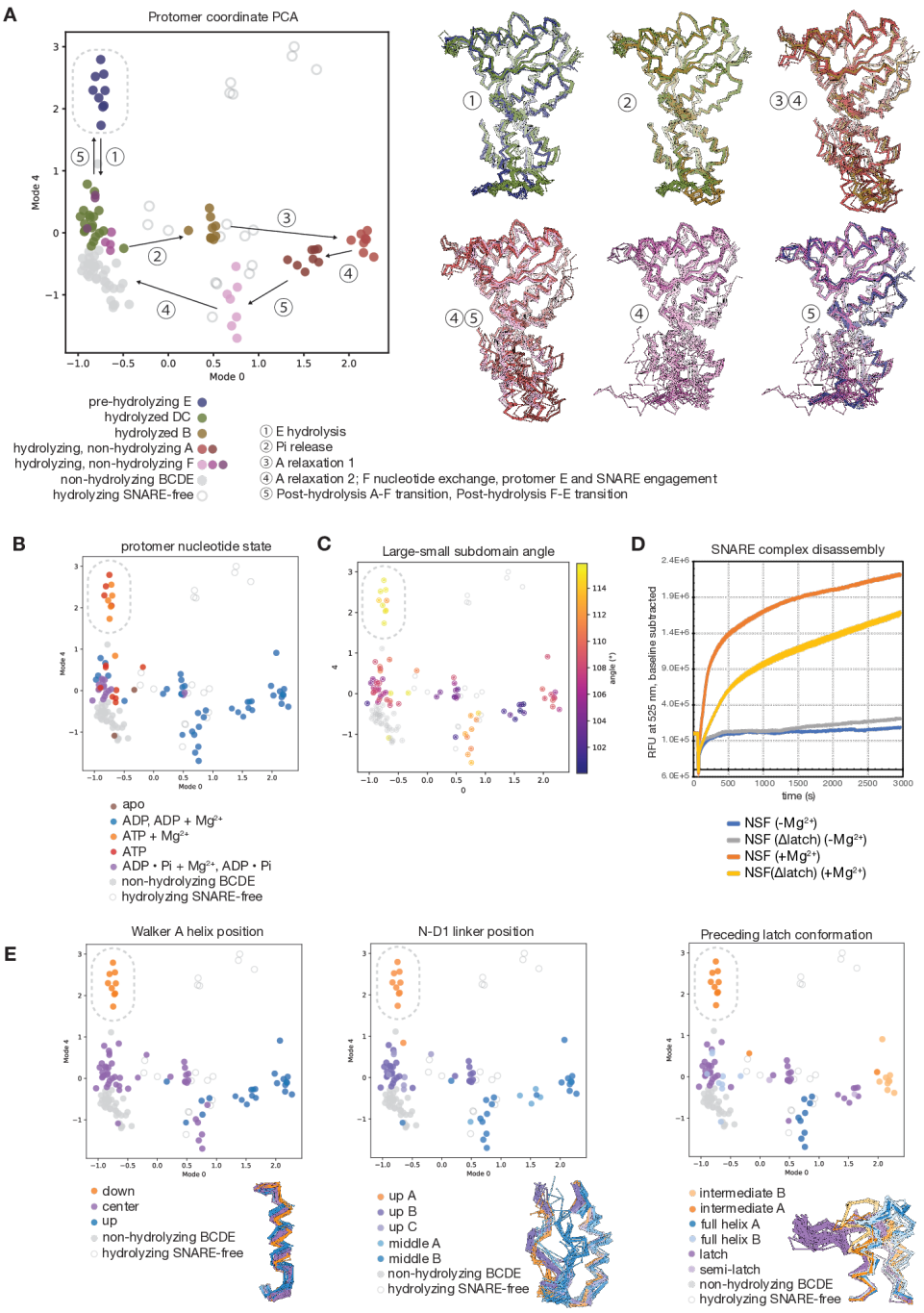

Figure 6 | Principal component analysis of NSF D1 protomer coordinates reveals further details related to sequential hydrolysis

A. 132 D1 domain models were aligned by large subdomain (residues 210–392), PCA was performed on Cα coordinates, and HDBSCAN was used to cluster the models in 11-dimensional space with a minimum cluster size of 3 models. Protomers cluster into discrete groups based on

628 conformation; these are easily distinguished upon projection into a 2D space defined by the first
629 and fifth modes. A proposed hydrolysis cycle connects these clusters as indicated by arrows
630 between clusters and descriptions below. Superimposed models corresponding to these
631 transitions are shown on the right. The cluster corresponding to pre-hydrolysis protomers E is
632 circled with a dashed line.

633 **B.** Protomer nucleotide state, mapped to the 2D PCA coordinate from **A**. The ATP + Mg^{2+} state is
634 unique to protomers E (top left, dashed line).

635 **C.** The angle (º) between helices α_3 and α_8 (a proxy for the relative angle between the D1 large
636 and small subdomains). Protomers E have the largest angle due (top left, dashed line).

637 **D.** A mutant form of NSF, NSF(Δlatch), was generated in which part of the latch loop (residues
638 460–466) was replaced with a short glycine-serine linker (SGS) and assayed for its ability to
639 disassemble the ternary SNARE complex composed of syntaxin, SNAP-25, and synaptobrevin,
640 relative to wild-type NSF as described previously[6]. Traces show the mean ± SEM of eight
641 replicates for each form of NSF, with and without adding $MgCl_2$ to initiate the reaction.
642 Disassembly rates were calculated by linear regression to each trace in the linear region of the
643 time course, from ~95–350 s, depending on the trace. NSF(Δlatch) disassembled SNARE
644 complex at 28 ± 1% the rate of wild type.

645 **E.** Three conformational features that distinguish the pre-hydrolysis protomer E cluster (top left,
646 dashed line), mapped to the 2D PCA coordinate from **A**. These features are in contact and
647 structurally coupled. The position of nucleotide in the active site is modulated by the position of
648 the Walker A helix (α_3), which occupies three discrete states; pre-hydrolysis protomers E occupy
649 the "down" state (left). The position of the helix is allosterically modulated by at least two

650 inputs. First, the N-D1 linker conformation (center) is connected to the state of N-domain
651 binding to α-SNAP, and it interacts with the latch loop of the up-ring protomer upon rebinding.
652 Second, the latch loop of the up-ring protomer contacts this region in *trans* and is also
653 structurally coupled (right). These two features push against the C-terminal end of the Walker A
654 helix and ultimately modulate the position of the ATP γ-phosphate relative to key catalytic
655 residues.

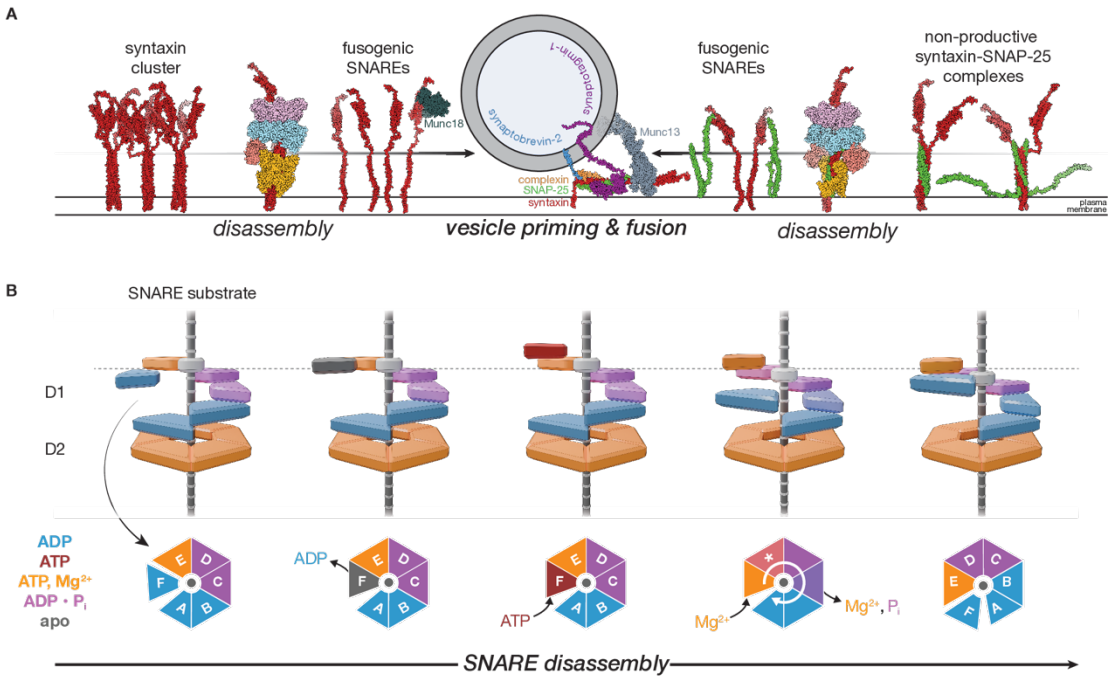

656

657 **Figure 7 | An expanded model for NSF action across cellular and atomic scales**

658 **A.** A model for disassembling non-fusogenic SNARE species by NSF and α-SNAP at the
659 presynapse and progression to priming and fusion. Syntaxin nanodomains comprised at least in
660 part of tetrameric syntaxin SNARE complexes serve as a reservoir for the liberation of
661 individual, fusogenic syntaxin molecules by NSF upon disassembly. These syntaxin molecules
662 may also enter non-productive binary complexes with SNAP-25, with 2:1 or 2:2 stoichiometry;
663 such complexes must also be disassembled by NSF to ensure *trans*-SNARE complex formation

664 with synaptobrevin on incoming synaptic vesicles in concert with other factors, such as Munc18,
665 Munc13, complexin, and synaptotagmin. Where possible, full-length structures (structures
666 reported here and PDB IDs 1N7S, 4JEU, 5W5C) were supplemented with AlphaFold2[60]
667 structures to provide additional context, and ISOLDE[61] was used with secondary structure
668 restraints to reposition flexible regions.

669 **B.** A sequential hydrolysis model for SNARE complex disassembly by NSF is inferred from
670 comparing different classes from non-hydrolyzing and hydrolyzing conditions. Following
671 hydrolysis-independent substrate side loading, the D1 ring is found in a pre-hydrolysis state with
672 ATP in protomer E of D1. Protomer F nucleotide exchange then enables ATP exchange and
673 rebinding to both SNARE substrate and the formation of the interprotomer interface with
674 protomer E, triggering ATP hydrolysis in protomer E and substrate translocation. This is
675 accompanied by P_i and Mg^{2+} release from down-ring protomers; in many structures, the release
676 occurs between protomers C and B. The cycle then begins anew. Blue corresponds to ADP-
677 bound, red to ATP-bound, purple to ADP•P_i bound, and grey to nucleotide-free. See Movie S1 for
678 an animated rendition.

679 # Methods

680 **PC12 transfection and imaging**

681 The PC12 cells, generously provided by Prof. Tobias Meyer from Stanford University, were
682 cultured on glass-bottomed dishes (MatTek; P35G-1.5-14-C) and allowed to adhere for 24 hr. To
683 introduce genetic material into the cells, transfection was performed using the TurboFect™
684 Transfection Reagent (#R0532, Thermo Fisher Scientific, USA) according to the manufacturer's
685 instructions. In brief, the plasmids (NSF-mScarlet-I plasmid: 1.75 μg; GFP-Syntaxin plasmid:

686 0.5 μg) were combined with 6.75 μL of TurboFect in 225 μL of DMEM medium (without FBS)
687 and incubated for 20 min. The DNA-TurboFect mixtures were carefully added drop-wise to the
688 cell cultures and incubated for 6 hr. Following the incubation, the cell cultures were replaced
689 with complete culture medium. After 24 hr post-transfection, the cells underwent three washes
690 with PBS. Subsequently, the cells were imaged using a structured illumination Nikon N-SIM
691 system (version AR5.11.00 64bit, Tokyo, Japan) equipped with an Apochromat 100×/1.49
692 numerical aperture oil-immersion objective lens. Using a 488 nm laser, the samples were excited
693 to acquire green SIM images, which captured emission within the 500–550 nm bandwidth,
694 specifically for GFP. Additionally, red SIM images were obtained by exciting the samples with a
695 561 nm laser to capture emission within the 570–640 nm bandwidth, corresponding to mScarlet-
696 I. To determine the degree of colocalization between syntaxin and NSF, Pearson's correlation
697 coefficient was calculated between channels *ImageJ*[62].

698 **Yeast imaging**

699 Super-resolution microscopy of *S. cerevisiae* expressing GFP-tagged Sso1 was performed using
700 structured illumination microscopy (SIM) on the OMX-Blaze system (Applied Precision,
701 Issaquah, WA). Glass-bottom dishes (1.5H, Cellvis) were pretreated with 0.01% poly-l-lysine by
702 adding 600–1000 μL to the center and incubated overnight. Following incubation, the dishes
703 were washed with deionized water to remove excess poly-l-lysine. Yeast cultures were grown
704 overnight, washed twice with phosphate-buffered saline (PBS), and resuspended to an optical
705 density (OD) of 0.4. A 10–20 μL volume of the yeast suspension was deposited onto the treated
706 dishes, followed by the addition of Diamond Antifade (Thermo Fisher Scientific) to prevent
707 photobleaching during imaging. The glass-bottom dishes were placed in a metal holder with 1–2
708 drops of immersion oil (refractive index 1.512) added before placement on the microscope stage.

709 SIM imaging was conducted using a laser appropriate for GFP excitation, and images were
710 captured with a 100× objective for a *z*-slice thickness of 0.125 µm, spanning a total thickness of
711 2.6 µm. Widefield images were also collected at 0.2 µm slice thickness when necessary.

712 **Protein expression and purification**

713 All NSF, the wild-type and mutant NSF-mScarlet-I, and NSF(Δ460–466) proteins were derived
714 from NSF from the Chinese hamster *C. griseus*, expressed in BL21(DE3)-RIL *E. coli*, and
715 purified as described previously[6], with final reassembly of hexameric NSF in reassembly buffer
716 (50 mM Tris pH 8.0, 150 mM NaCl, 1 mM EDTA, 1 mM ATP, and 1 mM TCEP). α-SNAP from
717 rat *R. norvegicus* was expressed in *E. coli* and purified as described previously[63]. Soluble rat
718 neuronal SNARE complex for the fluorescence-based disassembly assay (wild-type SNAP-25A,
719 syntaxin-1A 1–265, and 6×His-synaptobrevin-2 1–96) was purified by co-expression in C41 *E.*
720 *coli* and purified as described previously[63] Purified soluble rat neuronal SNARE complex was
721 fluorescently labeled with Oregon Green 488 maleimide dye as described previously[6].

722 Syntaxin-1A fragment 2-253 (Stx^{2-253}) was N-terminal His_6-tagged using the plasmid pTEV5.
723 Overexpression in *E. coli* BL21(DE3) was carried out in 8 L of auto-inducible media at 37ºC for
724 4 hr and then 30ºC overnight. Cells were collected by centrifugation; half of the pellet was
725 resuspended into 200 mL of 50 mM TRIS pH 8, 500 mM NaCl, and 10 mM imidazole and
726 supplemented with DNAse, lysozyme, 1 mM $MgCl_2$, and 2 eComplete Protease Inhibitor
727 Cocktail tablets (Roche). Cells were lysed by sonication (1 s on/3 s off, total 20 min, 55%
728 amplitude, 4ºC). Debris were removed by centrifugation at 43,000 rpm for 30 min at 4ºC using a
729 Ti45 rotor. The supernatant was then mixed with 5 mL of nickel-NTA agarose resin (Qiagen)
730 equilibrated with the lysis buffer. The suspension was gently stirred for 1 hr at 4ºC. The resin was
731 subsequently recovered by centrifugation at 4,200 rpm for 10 min at 4ºC, poured into a column,

732 and attached to an AKTA Start (Cytiva). An extensive wash was performed using 20 CV of 50
733 mM TRIS pH 8, 500 mM NaCl, and 40 mM imidazole until the 280 nm signal was stable.
734 Protein was eluted in 1 mL fractions in 50 mM TRIS pH8, 200 mM NaCl, and 400 mM
735 imidazole. Syntaxin-enriched fractions were identified by SDS-PAGE and pooled. To remove the
736 His-tag, the protein was mixed with an excess of TEV protease and dialyzed against 20 mM
737 HEPES pH 7.5, 50 mM NaCl, 1 mM DTT, overnight at 4ºC. The sample was centrifuged at
738 4,000 rpm for 10 min at 4ºC, filtered, and loaded onto a Mono-Q 5/50 column attached to an
739 AKTA Pure (Cytiva). The resin was extensively washed with 20 mM HEPES pH 7.5, 50 mM
740 NaCl, 0.2 mM EDTA until 280 nm signal was stable. Elution was performed in 120 CV over 2 hr
741 from 0.050–1 M NaCl. 2 mL fractions within the major peaks were run on SDS-PAGE, and
742 fractions containing Stx^{2-253} were concentrated using a 10 kDa cutoff centrifugal filtration device.
743 The concentrate was filtered and further purified using a Superdex Increase 75 16/60 column
744 (Cytiva) equilibrated with 20 mM TRIS pH 8, 150 mM NaCl. Fractions were run on an SDS-
745 PAGE, and fractions containing Stx^{2-253} were concentrated using a 10 kDa MWCO centrifugal
746 filtration device. A final concentration of 745 mM was determined by using the extinction
747 coefficient 5,960 M^{-1} cm^{-1}. Stx^{2-253} was aliquoted, flash frozen, and stored at -80ºC until further
748 use. An independent sample purified from the same batch of cells was analyzed on MALDI-TOF,
749 and a monomeric molecular weight of 29,208.50 g/mol was confirmed.

750 Binary neuronal SNARE complex for cryo-EM imaging studies (SNAP-25A with all cysteines
751 mutated to serine, syntaxin-1A 1–267) was purified following co-expression of SNARE proteins
752 from *E. coli* BL21 STAR (Invitrogen). Cells were grown overnight at 30°C using an auto-
753 inducing LB medium[64]. After harvesting the cells by centrifugation, the pellet was resuspended
754 in lysis buffer (50 mM NaPi pH 8.0, 300 mM NaCl, 20 mM imidazole, 0.5 mM TCEP)

755 supplemented with lysozyme, DNase I, and antiprotease tablets (Roche) and subjected to
756 sonication (3 s on, 9 s off, 60% power for 5 min, repeated 3×) and centrifugation (10,000 rpm for
757 10 min followed by 43,000 rpm for 40 min). The clarified lysate was bound to Ni-
758 NTA agarose beads (QIAGEN) equilibrated in a lysis buffer. Beads were harvested by
759 centrifugation (2200 rpm for 10 min), poured into a gravity column, and washed with lysis
760 buffer, urea buffer (50 mM NaP_i pH 8.0, 300 mM NaCl, 30 mM imidazole, 0.5 mM TCEP, 7.5 M
761 urea), and wash buffer (50 mM NaPi pH 8.0, 300 mM NaCl, 30 mM imidazole, 0.5 mM TCEP).
762 The SNARE complex was then eluted with wash buffer supplemented with an additional
763 320 mM imidazole. The fresh eluent of the Ni-NTA affinity purified SNARE complex was
764 supplemented with tobacco etch virus (TEV) protease and dialyzed against buffer A1 (50 mM
765 Tris-HCl, pH 8.0, 250 mM NaCl, 0.5mM TCEP) overnight at 4°C. After dialysis, the sample was
766 diluted to a final NaCl concentration of 50 mM using buffer A1 without NaCl, and the His-tag-
767 free complex was subjected to anion exchange chromatography (Buffer A2: 50 mM Tris-HCl, pH
768 8.0, 50 mM NaCl, 0.5 mM TCEP; Buffer B1: 50 mM Tris-HCl, pH 8.0, 500 mM NaCl, 0.5 mM
769 TCEP) using a MonoQ 4.6/100 column (Cytiva) and a linear gradient of NaCl starting at 50 mM
770 and ending at 500 mM. The peaks containing the purified complex were pooled and loaded onto
771 a Superdex 75 16/60 column to normalize NaCl concentration (50 mM Tris-HCl pH 8.0, 50 mM
772 NaCl, 0.5 mM TCEP).

773 The sx20S supercomplex was formed by mixing ATP-bound NSF, α-SNAP, and syntaxin to a
774 ratio of 1:5:30 in reassembly buffer and purifying it by size-exclusion chromatography using a
775 Superose 6 10/300 GL column; the first peak to elute was collected and concentrated to around
776 15 mg mL^{-1} for vitrification and cryo-EM imaging. The 21bin20S supercomplex was purified
777 similarly but with a 1:5:30 ratio of NSF:binary SNARE complex:α-SNAP. In the case of

778 preparing 21bin20S supercomplex for imaging under hydrolyzing conditions, EDTA was omitted
779 from the final SEC buffer.

780 **Gel-based syntaxin disassembly assay**

781 Soluble syntaxin (2–253) and α-SNAP were mixed at concentrations of 100 μM and 150 μM,
782 respectively, in 50 mM Tris pH 8.0, 150 mM NaCl, 1 mM TCEP, and 1 mM EDTA (SEC buffer)
783 and incubated for 20 min. NSF was subsequently added to a final concentration of 2.5 μM,
784 bringing the total reaction volume to 500 μL. The mixture was then injected into a Superdex 200
785 16/60 column (Cytiva) and complex peak fractions were pooled and concentrated using a
786 100,000 MWCO filtration device. For each assay condition, 5 μg of complex was used. Two
787 experimental conditions were performed in triplicate; either EDTA or $MgCl_2$ was added to a final
788 concentration of 4 mM. Samples were incubated for 20 min at room temperature and re-
789 concentrated using 100k MWCO filters before SDS-PAGE. Re-concentration effectively de-
790 enriches liberated syntaxin and α-SNAP molecules. Densitometry was performed using
791 *ImageJ*[62], and statistical significance was established between the conditions using a two-tailed
792 Student's *t*-test.

793 **Gel-based ternary SNARE complex disassembly assay**

794 To verify that NSF activity was not hampered by the C-terminal addition of mScarlet-I, SNARE
795 complex disassembly was evaluated by gel electrophoresis. NSF, NSF-mScarlet-I, α-SNAP, and
796 the neuronal SNARE complex were dialyzed into 25 mM TRIS pH 8, 150 mM NaCl, 1 mM ATP.
797 Then, components were combined into either EDTA buffer (25 mM TRIS pH 8, 2 mM ATP, 1
798 mM EDTA) or Mg^{2+} buffer (25 mM TRIS pH 8, 2 mM ATP, 4 mM $MgCl_2$). The reaction volume
799 was 10 μL, and contained 500 nM NSF or NSF-mScarlet-I and 50 nM α-SNAP. Assays were
800 started by adding 10 μM SNARE complex, and samples were then incubated at 37ºC for 10 min

801 in a thermocycler. 2 uL of 5×-Laemli loading buffer was then added, and samples were
802 incubated at 95ºC for 5 min. Finally, 5 µL of each reaction was loaded onto an AnykD TGX gel
803 (BioRad) and run at 200 V for 45 min. The gel was stained with Coomassie R-250 (BioRad). As
804 internal controls, all single components were diluted at a similar concentration as the reactions
805 using Mg^{2+} buffer and treated in parallel. Note that the additional control marked as "SNARE
806 complex unboiled" corresponds to the SNARE complex incubated at 37ºC but not at 95ºC after
807 adding loading buffer. For reference, monomeric NSF is ~83 kDa while NSF-mScarlet-I is ~112
808 kDa.

809 **Fluorescence dequenching-based neuronal SNARE complex disassembly assay**

810 The details of the fluorescence dequenching assay have been previously described[6,32,38,40,41,63].
811 Fluorescence dequenching assays were carried out using a FlexStation II 384-well plate reader
812 (Molecular Devices) with a final reaction volume of 60 µL in 20 mM Tris pH 8, 100 mM NaCl, 2
813 mM ATP, and 0.5 mM TCEP. The assay plate was first prepared by adding 50 µL of 60 nM wild-
814 type or Δ460–466 mutant NSF, 2.4 µM α-SNAP, 480 nM OG-labeled neuronal SNARE complex
815 in reaction buffer to each well. Then, 100 µL of reaction buffer (as a control) or ATP hydrolysis
816 initiation buffer (reaction buffer supplemented with 24 µM $MgCl_2$) was added to appropriate
817 wells of the compound plate, and fluorescence dequenching was monitored. Excitation was
818 performed at 485 nm, and emission was monitored at 525 nm with a dichroic mirror at 515 nm.
819 First, fluorescence intensity was monitored before reaction initiation for 60 s. Then, 10 µL of
820 compound plate solution was transferred to each assay plate well (diluting all protein 5/6-fold
821 and $MgCl_2$ concentrations six-fold) and triturated, initiating the disassembly reaction. The final
822 protein concentrations following mixing were 50 nM NSF, 2.0 µM α-SNAP, and 400 nM
823 SNARE complex. The final $MgCl_2$ concentration was 4 mM. Dequenching was then monitored

824 for 30 min at 20 ºC. Linear regression over the first several minutes was performed to estimate
825 relative disassembly rates. The statistical significance of changes to disassembly rates was
826 assessed using the two-tailed Student's *t*-test.

827 **Sample vitrification for cryo-EM SPA**

828 The samples were prepared immediately before vitrification (Fig. S2). Quantifoil R1.2/1.3 200
829 mesh gold grids (Quantifoil Micro Tools GmbH, Germany) were cleaned with chloroform, dried
830 for several hours, and subjected to glow discharge using a PELCO easiGlow Glow Discharge
831 Cleaning System (Ted Pella) under vacuum at 15 mA for 45 s with a 15 s hold time. Immediately
832 following 21bin20S or sx20S supercomplex purification, proteins were concentrated to ~15 mg
833 mL^{-1} in 17 µL. For the hydrolyzing condition, 2 µL of 10 × ATP Regeneration Solution (50 mM
834 Tris pH 8.0, 150 mM NaCl, 1 mM ATP, 160 mM creatine phosphate, and 0.3 mg/mL rabbit
835 muscle creatine kinase (Roche)) was added, and the sample was incubated on ice for 2 min; in
836 contrast, 2 µL of reassembly buffer was added in the case of non-hydrolyzing conditions. Then,
837 for the hydrolyzing condition, 1 µL of 20 × Reaction Initiation Solution (50 mM Tris pH 8.0, 150
838 mM NaCl, 1 mM ATP, 20 mM MgCl2, 1% Nonidet P-40) was added, otherwise 1 µL of 1%
839 Nonidet P-40 was added in the case of non-hydrolyzing conditions. Using a Vitrobot Mark IV
840 (Thermo Fisher Scientific), 4 µL of a given sample was applied to a grid at room temperature
841 and 100% humidity and, blotted for 4 s with a blot force of 3, and subsequently plunge-frozen in
842 liquid ethane.

843 **Cryo-EM SPA data collection**

844 Grids were imaged using a Titan Krios electron microscope (Thermo Fisher Scientific) operated
845 at 300 kV and equipped with a K3 camera (Gatan). Data collection was performed using
846 *SerialEM*[65]. All datasets were collected with a nominal magnification of 22,500× for a physical

847 pixel size of 1.096 Å and a super-resolution pixel size of 0.548 Å. Dose rate was either ~10 or
848 ~20 e^-/px/s depending on whether correlated double sampling (CDS) was enabled on the K3, for
849 a total dose of around 30 $e^-/Å^2$. Nine grid holes were imaged for each stage movement using
850 multiple record setup in *SerialEM*, with one collection per hole. At each hole, either a 2 s or 4 s
851 exposure fractionated into either 40 or 80 frames was collected, depending on whether CDS was
852 enabled. Defocus values ranged from -1–-3 µm. See Table S1 for details.

853 **Cryo-EM SPA image processing**

854 All cryo-EM datasets were processed using a software pipeline consisting of *MotionCorr2*[66],
855 *CTFFIND4*[67], *RELION 3*[68,69], and *cryoSPARC*[51,70]. Early-stage processing was carried out in
856 *RELION 3*, with final 3D refinement and variability analysis carried out with *CryoSPARC*.
857 Dataset-specific processing schemes are presented in Figs. S3–7. Generally, all processing
858 proceeded as follows. Processing began in *RELION 3*, with per-micrograph optics groups
859 defined for a given dataset based on the nine beam shift positions using the custom script
860 *update_relion_tilt_class_og.py*. For example, the hydrolyzing condition micrographs were
861 collected in two sessions, so 18 total optics groups were defined. The raw image stacks were
862 dose-weighted and motion-corrected using the *RELION* implementation of *MotionCorr2*, with
863 seven patches along the *x* direction and five patches along *y*. CTF parameters were estimated for
864 each micrograph using *CTFFIND4* with a resolution range of 3–30 Å, an FFT box size of 1024
865 px, and otherwise default parameters. Micrographs were then selected based on maximum
866 resolution and the CTF figure of merit.

867 Generally, an initial round of manual picking, extraction, and 2D classification were used to
868 assess data set quality and provide particles to reconstruct an initial 3D model. Good particles
869 from manual picking were then used for automated particle picking in *RELION*. Particles were

870 then extracted with a box size of 640 px, binned 8× (4.384 Å Å pixel size) to a box size of 80 px,
871 and subjected to at least one round of 2D classification to eliminate obviously bad particles.
872 Next, multiple rounds of 3D classification with a 280 Å mask diameter and a regularization
873 parameter $T = 4$ were performed over many iterations to determine the proper number of discrete
874 states in a given dataset, and to ensure that particles were classified properly. Convergence of
875 classification was monitored with a custom script, *startle.py*. Several classes slightly larger than
876 the number of discrete states were used, and classes that appeared to lie along a continuous
877 conformational coordinate were subsequently re-merged into a single class. In the case of the
878 hydrolyzing dataset, SNARE substrate-bound and SNARE substrate-free particles were split into
879 separate groups of particles, re-classified, and processed independently.

880 Following classification, particles were re-centered and re-extracted with a box size of 588 px
881 and binned 2× (1.096 Å pixel size) with a box size of 294 px. Following an initial round of 3D
882 refinement and post-processing, CTF refinement was performed. Typically, defocus,
883 astigmatism, B-factor, tilt, and trefoil were refined on a per-particle or per-micrograph basis,
884 depending on the specific class. Particles were then subjected to an additional round of 3D
885 refinement and post-processing, and optimal parameters for particle polishing were determined
886 by training on several classes, yielding different parameter sets. Particle polishing was then
887 performed with these sets, and 3D refinement and post-processing were used to assess the
888 results. Polished particles were then subjected to a final round of 3D refinement, post-processing,
889 and CTF refinement, during which anisotropic magnification was estimated. At this stage,
890 particles and 3D reconstructions were imported into *CryoSPARC* for a final round of non-
891 uniform refinement, which typically improved the quality of reconstructions.

892 In the case of one class observed under hydrolyzing conditions (c4-7-16-20-24), a large degree of
893 continuous heterogeneity was observed. 3D variability analysis (3DVA) revealed a trajectory of
894 protomer F nucleotide and rebinding, so particles in the first mode were split using a custom
895 script, *split_by_3dva.py*, as current tools to do so natively were unavailable at the time. This
896 script fits a normal distribution to the eigenvector magnitude distribution and allows slicing with
897 different cutoffs. For the 3DVA subclasses (slices O and P), particles in the ±1.5 σ tails of the
898 distribution were used for reconstruction.

899 These reconstructions were considered final for the overall 20S architecture, but further
900 processing was required to generate local reconstructions of the various α-SNAP—SNARE
901 subcomplexes. In the case of the sx20S dataset, only one class was observed with ordered spire
902 density, so local refinement was relatively simple. *CryoSPARC* signal subtraction
903 (*particle_subtract*; masks generated using *Segger* 2.5.3[71] in *Chimera* 1.15[72]) was used to remove
904 the signal from NSF N, D1, and D2 domains, leaving only the α-SNAP—syntaxin H3 SNARE
905 domain tetramer subcomplex. Local refinement (*new_local_refine*) was then performed on these
906 particles with a 40º/20 Å search extent and a custom fulcrum at the N-terminal end of the
907 SNARE bundle near the point of interaction with the F protomer of the D1 ring. The resulting
908 volumes were re-centered on the center of mass (*volume_alignment_tools*), and particle
909 alignments were updated as well (*align_3D*). Then, a final round of local refinement
910 (*new_local_refine*) was performed with the map center as the fulcrum (the default setting), a
911 smaller search extent of 10º/5 Å, and a maximum alignment resolution of 0.1º. Per-particle scales
912 were also reset, and minimization was performed over a per-particle scale. This produced the
913 final reconstruction of this subcomplex for subsequent modeling. In the case of the α-SNAP—
914 2:1 and α-SNAP—2:2 binary SNARE subcomplexes, this procedure was followed for each class

915 meeting certain criteria (number of particles, ordered spire, resolution), yielding five local
916 reconstructions for the α-SNAP—2:1 binary SNARE subcomplex and six local reconstructions
917 for the α-SNAP—2:2 binary SNARE subcomplex. In each case, these reconstructions were re-
918 centered (*volume_alignment_tools*), aligned to one another with the center of mass at the origin
919 (*align_3D)*, and a final round of local refinement was run to produce a final higher-resolution
920 reconstruction incorporating data from multiple classes. This produced the final reconstruction of
921 these subcomplexes for subsequent modeling. For more details about all data sets, see Figs. S3–
922 7, Tables S1–2, and Fig. S8.

923 **Model building and refinement**

924 All manual model building and refinements were carried out using *Coot*[73]. Semi-manual
925 refinement into low-resolution features was performed with *UCSF ChimeraX*[74] and the
926 *ISOLDE*[61] plugin. Automated refinement was performed using *phenix.real_space_refine*[75,76].

927 First, models of the three α-SNAP—SNARE subcomplexes were built by rigid body fitting of
928 the best possible starting models into their corresponding densities using *UCSF ChimeraX*. In
929 each case, 3–4 copies of a high-quality α-SNAP model from the previous best 20S model (PDB
930 ID 6MDM[6]) were rigid body fit into the density. In the case of the syntaxin H3 domain tetramer
931 complex, four copies of the syntaxin chain from the high-resolution crystal structure (PDB ID
932 1N7S[49]) of the neuronal SNARE complex were docked into the density, with several
933 characteristic residues as fiducials. The quality of the local reconstructions of the SNARE—α-
934 SNAP spires allowed unique assignment of the identity of the SNARE domains, their
935 directionality, and register (Figs. 2D, 3D, 4D, Fig. S7DE, Fig. S9A). In the case of the 2:1 binary
936 SNARE complex, the syntaxin and SNAP-25 components of the same crystal structure were
937 docked into the density, but with the SNARE domain of synaptobrevin replaced with an

938 additional syntaxin H3 SNARE domain; key side chain densities as well as a distinctive kink
939 leading into the SNAP-25 SN2 domain guided placement (Fig. 3C, Fig. S9A). In the case of the
940 2:2 binary SNARE complex, a previous crystal structure (PDB ID 1JTH[34]) was docked into the
941 density without modification. In all cases, individual components were trimmed, or residues
942 were added where supported by the density. A round of *phenix.real_space_refine* was then
943 performed with only rigid-body refinement enabled for each component. Subsequent cycles of
944 manual model building were performed in *Coot* and *ISOLDE* followed by 1–7 macrocycles of
945 *phenix.real_space_refine* with global minimization and local grid search enabled. Ramachandran
946 and secondary structure restraints were used throughout.

947 Models of NSF or the different 20S supercomplexes were then built. Gold-standard models were
948 first built into two high-resolution NSF classes from a single non-hydrolyzing dataset with near-
949 atomic resolutions using the previous best model of NSF (PDB ID 6MDM[6]) as a starting model.
950 The starting model was first docked into cryo-EM density using ChimeraX. Next, a round of
951 *phenix.real_space_refine* was performed with only rigid-body refinement enabled; each large
952 and small subdomain of each protomer was treated as a single rigid body (twelve total).
953 Nucleotides and water molecules were then added where appropriate. Subsequent cycles of
954 manual model building were performed in *Coot* and *ISOLDE* followed by 1–7 macrocycles of
955 *phenix.real_space_refine* with global minimization and local grid search enabled. Ramachandran
956 and secondary structure restraints were used throughout.

957 The previously described models were then used as starting models in building the sx20S and
958 bin20S supercomplexes. In sx20S and bin20S reconstructions with well-defined N-domains (i.e.,
959 a recognizable two-lobed density), one or more instances of the re-processed model derived from
960 the crystal structure (PDB ID 1QCS[77]) as re-processed by *PDB_REDO*[78] were rigid body fit into

961 density before refinement. Next, the appropriate α-SNAP—SNARE subcomplex was docked
962 into the density, completing the spire structure. A round of *phenix.real_space_refine* was
963 performed with only rigid-body refinement enabled; each large and small subdomain of each
964 protomer, each N domain, and each α-SNAP—SNARE subcomplex was treated as a rigid body
965 (for a 20S particle with four engaged N-domains, this would be 17 total rigid body groups).
966 Nucleotides, Mg^{2+}, P_i, and water molecules were then added where appropriate. Subsequent
967 cycles of manual model building were performed in *Coot* and *ISOLDE* followed by 1–7
968 macrocycles of *phenix.real_space_refine* with global minimization and local grid search enabled.
969 Ramachandran and secondary structure restraints were used throughout.

970 All model figures were prepared with *UCSF ChimeraX*, in many cases with custom CXC scripts
971 generated by the Python scripts described below.

972 **Automated NSF model analysis and coordinate PCA**

973 Several custom Python scripts (*preprocess_models.py, analyze_models.py*) using the *Bio.PDB*
974 module[79] of the Biopython project[80] as well as *pandas*[81], *numpy*[82], *scipy*[83], *scikit-learn*[84], and
975 *matplotlib*[85] were used to standardize all 25 NSF, sx20S, or bin20S models for further analysis,
976 such as to perform principle components analysis (PCA) and HDBSCAN clustering, to measure
977 NSF D1 large-small subdomain angles, to perform planarity fits for NSF domains and
978 subdomains, to measure distances between key catalytic residues and nucleotides, and to map
979 various values to structures for visualization in *UCSF ChimeraX*.

980 For PCA, 132 NSF D1 domains from 22 models over all datasets were split into large and small
981 subdomains, which were then aligned to one another (large, residues 224–373; small, residues
982 400–486) using *Bio.PDB.Superimposer*. Splitting removes the largest source of variance in the

983 data, the rigid body motions of the two subdomains relative to each other, which is considered
984 trivial for the purposes of this analysis. Next, a Cα coordinate matrix **C** with dimensions $n_{models} \times$
985 $n_{residues} \times 3$ was constructed for residues shared by all models and flattened into two dimensions,
986 creating $\mathbf{C_{flat}}$ with n_{models} rows and $n_{residues} \times 3$ columns. $\mathbf{C_{flat}}$ was then rescaled using
987 *sklearn.preprocessing.StandardScaler* and PCA was performed on $\mathbf{C_{flat}}$ using
988 *sklearn.decomposition.PCA*. 13 components were found to contribute 99% of the variance, so a
989 transformed matrix $\mathbf{C_{trans}}$ with dimensions $n_{models} \times 13$, with eigenvectors sorted along the second
990 axis by eigenvalue, was calculated. The cluster analysis of models was then performed using
991 *sklearn.cluster.HDBSCAN* with a minimum cluster size of three, producing 11 clusters
992 accounting for 119/132 total models. This analysis serves as the basis for Fig. 6A.

993 For NSF D1 and D2 plane fits, centers of mass for all subdomains were calculated, and the
994 planes for different combinations of these points were fit using a least squares approach (Fig.
995 S11). For NSF D1 large-small subdomain angle calculations, the primary axes of two α-helices
996 in the large (residues 350–358) and small subdomains (residues 442–452) were calculated by
997 singular value decomposition using *np.linalg.svd*, with implementation inspired by
998 *helix_analysis.py* from the MDAnalysis package[86]. Vectors corresponding to these helical axes *u*
999 and *v* were normalized and centered at the coordinate origin, and the angle between them was
1000 calculated as $\theta = 2 \times \tan^{-1}\left(\sqrt{\sum_i \vec{u}_i^2}\sqrt{\sum_i \vec{v}_i^2}\right)$.

1001 Distances between key active site atoms over all models (Fig. S13) were calculated using
1002 *np.linalg.norm*, where the norm of the difference vector of the coordinates of each atom is the
1003 distance between them in Å. Significant changes in protomer E active site residues relative to the
1004 other five protomers were assessed by pairwise application of the Welch's t-test assuming non-

equal variances as implemented in *scipy.stats.ttest_ind*. Distance distributions were considered statistically different if $p < 0.05$.

All these values, as well as manually curated, qualitative data labels, were plotted in various ways using *matplotlib* or incorporated into automatically generated UCSF ChimeraX CXC scripts.

References

1. Rizo, J., and Südhof, T.C. (2012). The membrane fusion enigma: SNAREs, Sec1/Munc18 proteins, and their accomplices--guilty as charged? Annu. Rev. Cell Dev. Biol. *28*, 279–308. https://doi.org/10.1146/annurev-cellbio-101011-155818.

2. Brunger, A.T., Choi, U.B., Lai, Y., Leitz, J., and Zhou, Q. (2018). Molecular Mechanisms of Fast Neurotransmitter Release. Annu. Rev. Biophys. *47*, 469–497. https://doi.org/10.1146/annurev-biophys-070816-034117.

3. Leitz, J., Wang, C., Esquivies, L., Pfuetzner, R.A., Peters, J.J., Couoh-Cardel, S., Wang, A.L., and Brunger, A.T. (2024). Beyond the MUN domain, Munc13 controls priming and depriming of synaptic vesicles. Cell Rep. *43*. https://doi.org/10.1016/j.celrep.2024.114026.

4. Brunger, A.T., Choi, U.B., Lai, Y., Leitz, J., White, K.I., and Zhou, Q. (2019). The pre-synaptic fusion machinery. Curr. Opin. Struct. Biol. *54*, 179–188. https://doi.org/10.1016/j.sbi.2019.03.007.

5. Rizo, J. (2022). Molecular Mechanisms Underlying Neurotransmitter Release. Annu. Rev. Biophys. *51*, 377–408. https://doi.org/10.1146/annurev-biophys-111821-104732.

6. White, K.I., Zhao, M., Choi, U.B., Pfuetzner, R.A., and Brunger, A.T. (2018). Structural principles of SNARE complex recognition by the AAA+ protein NSF. eLife *7*, e38888. https://doi.org/10.7554/eLife.38888.

7. Zhao, M., Wu, S., Zhou, Q., Vivona, S., Cipriano, D.J., Cheng, Y., and Brunger, A.T. (2015). Mechanistic insights into the recycling machine of the SNARE complex. Nature *518*, 61–67. https://doi.org/10.1038/nature14148.

8. Rickman, C., Medine, C.N., Dun, A.R., Moulton, D.J., Mandula, O., Halemani, N.D., Rizzoli, S.O., Chamberlain, L.H., and Duncan, R.R. (2010). t-SNARE Protein Conformations Patterned by the Lipid Microenvironment. J. Biol. Chem. *285*, 13535–13541. https://doi.org/10.1074/jbc.M109.091058.

1035 9. Murray, D.H., and Tamm, L.K. (2009). Clustering of Syntaxin-1A in Model Membranes is
1036 Modulated by Phosphatidylinositol-4,5-bisphosphate and Cholesterol. Biochemistry *48*,
1037 4617–4625. https://doi.org/10.1021/bi9003217.

1038 10. Aoyagi, K., Sugaya, T., Umeda, M., Yamamoto, S., Terakawa, S., and Takahashi, M. (2005).
1039 The activation of exocytotic sites by the formation of phosphatidylinositol 4,5-bisphosphate
1040 microdomains at syntaxin clusters. J. Biol. Chem. *280*, 17346–17352.
1041 https://doi.org/10.1074/jbc.M413307200.

1042 11. Lang, T., Bruns, D., Wenzel, D., Riedel, D., Holroyd, P., Thiele, C., and Jahn, R. (2001).
1043 SNAREs are concentrated in cholesterol-dependent clusters that define docking and fusion
1044 sites for exocytosis. EMBO J. *20*, 2202–2213. https://doi.org/10.1093/emboj/20.9.2202.

1045 12. Emperador-Melero, J., and Kaeser, P.S. (2020). Assembly of the presynaptic active zone.
1046 Curr. Opin. Neurobiol. *63*, 95–103. https://doi.org/10.1016/j.conb.2020.03.008.

1047 13. Weimbs, T., Low, S.H., Chapin, S.J., Mostov, K.E., Bucher, P., and Hofmann, K. (1997). A
1048 conserved domain is present in different families of vesicular fusion proteins:
1049 A new superfamily. Proc. Natl. Acad. Sci. U. S. A. *94*, 3046–3051.

1050 14. Bennett, M.K., Calakos, N., and Scheller, R.H. (1992). Syntaxin: A Synaptic Protein
1051 Implicated in Docking of Synaptic Vesicles at Presynaptic Active Zones. Science *257*, 255–
1052 259. https://doi.org/10.1126/science.1321498.

1053 15. Sutton, R.B., Fasshauer, D., Jahn, R., and Brunger, A.T. (1998). Crystal structure of a
1054 SNARE complex involved in synaptic exocytosis at 2.4 Å resolution. Nature *395*, 347–353.
1055 https://doi.org/10.1038/26412.

1056 16. Fernandez, I., Ubach, J., Dulubova, I., Zhang, X., Südhof, T.C., and Rizo, J. (1998). Three-
1057 Dimensional Structure of an Evolutionarily Conserved N-Terminal Domain of Syntaxin 1A.
1058 Cell *94*, 841–849. https://doi.org/10.1016/s0092-8674(00)81742-0.

1059 17. Sieber, J.J., Willig, K.I., Kutzner, C., Gerding-Reimers, C., Harke, B., Donnert, G.,
1060 Rammner, B., Eggeling, C., Hell, S.W., Grubmüller, H., et al. (2007). Anatomy and
1061 Dynamics of a Supramolecular Membrane Protein Cluster. Science *317*, 1072–1076.
1062 https://doi.org/10.1126/science.1141727.

1063 18. Bar-On, D., Wolter, S., Van De Linde, S., Heilemann, M., Nudelman, G., Nachliel, E.,
1064 Gutman, M., Sauer, M., and Ashery, U. (2012). Super-resolution Imaging Reveals the
1065 Internal Architecture of Nano-sized Syntaxin Clusters. J. Biol. Chem. *287*, 27158–27167.
1066 https://doi.org/10.1074/jbc.M112.353250.

1067 19. Knowles, M.K., Barg, S., Wan, L., Midorikawa, M., Chen, X., and Almers, W. (2010). Single
1068 secretory granules of live cells recruit syntaxin-1 and synaptosomal associated protein 25
1069 (SNAP-25) in large copy numbers. Proc. Natl. Acad. Sci. *107*, 20810–20815.
1070 https://doi.org/10.1073/pnas.1014840107.

1071 20. Wan, L., Chen, X., and Almers, W. (2021). Munc18-dependent and -independent clustering
1072 of syntaxin in the plasma membrane of cultured endocrine cells. Proc. Natl. Acad. Sci. *118*,
1073 e2025748118. https://doi.org/10.1073/pnas.2025748118.

1074 21. Ullrich, A., Böhme, M.A., Schöneberg, J., Depner, H., Sigrist, S.J., and Noé, F. (2015).
1075 Dynamical Organization of Syntaxin-1A at the Presynaptic Active Zone. PLOS Comput.
1076 Biol. *11*, e1004407. https://doi.org/10.1371/journal.pcbi.1004407.

1077 22. Barg, S., Knowles, M.K., Chen, X., Midorikawa, M., and Almers, W. (2010). Syntaxin
1078 clusters assemble reversibly at sites of secretory granules in live cells. Proc. Natl. Acad. Sci.
1079 *107*, 20804–20809. https://doi.org/10.1073/pnas.1014823107.

1080 23. Sakamoto, H., Ariyoshi, T., Kimpara, N., Sugao, K., Taiko, I., Takikawa, K., Asanuma, D.,
1081 Namiki, S., and Hirose, K. (2018). Synaptic weight set by Munc13-1 supramolecular
1082 assemblies. Nat. Neurosci. *21*, 41–49. https://doi.org/10.1038/s41593-017-0041-9.

1083 24. Pertsinidis, A., Mukherjee, K., Sharma, M., Pang, Z.P., Park, S.R., Zhang, Y., Brunger, A.T.,
1084 Südhof, T.C., and Chu, S. (2013). Ultrahigh-resolution imaging reveals formation of
1085 neuronal SNARE/Munc18 complexes in situ. Proc. Natl. Acad. Sci. *110*, E2812–E2820.
1086 https://doi.org/10.1073/pnas.1310654110.

1087 25. Yin, P., Gandasi, N.R., Arora, S., Omar-Hmeadi, M., Saras, J., and Barg, S. (2018). Syntaxin
1088 clusters at secretory granules in a munc18-bound conformation. Mol. Biol. Cell *29*, 2700–
1089 2708. https://doi.org/10.1091/mbc.E17-09-0541.

1090 26. Lang, T. (2007). SNARE proteins and 'membrane rafts.' J. Physiol. *585*, 693–698.
1091 https://doi.org/10.1113/jphysiol.2007.134346.

1092 27. Bademosi, A.T., Lauwers, E., Padmanabhan, P., Odierna, L., Chai, Y.J., Papadopulos, A.,
1093 Goodhill, G.J., Verstreken, P., van Swinderen, B., and Meunier, F.A. (2016). In vivo single-
1094 molecule imaging of syntaxin1A reveals polyphosphoinositide- and activity-dependent
1095 trapping in presynaptic nanoclusters. Nat. Commun. *7*, 13660.
1096 https://doi.org/10.1038/ncomms13660.

1097 28. Sieber, J.J., Willig, K.I., Heintzmann, R., Hell, S.W., and Lang, T. (2006). The SNARE Motif
1098 Is Essential for the Formation of Syntaxin Clusters in the Plasma Membrane. Biophys. J. *90*,
1099 2843–2851. https://doi.org/10.1529/biophysj.105.079574.

1100 29. Hanson, P.I., Otto, H., Barton, N., and Jahn, R. (1995). The N-Ethylmaleimide-sensitive
1101 Fusion Protein and α-SNAP Induce a Conformational Change in Syntaxin (*). J. Biol. Chem.
1102 *270*, 16955–16961. https://doi.org/10.1074/jbc.270.28.16955.

1103 30. Stepien, K.P., Prinslow, E.A., and Rizo, J. (2019). Munc18-1 is crucial to overcome the
1104 inhibition of synaptic vesicle fusion by αSNAP. Nat. Commun. *10*, 4326.
1105 https://doi.org/10.1038/s41467-019-12188-4.

1106 31. Ma, C., Su, L., Seven, A.B., Xu, Y., and Rizo, J. (2013). Reconstitution of the vital functions
1107 of Munc18 and Munc13 in neurotransmitter release. Science *339*, 421–425.
1108 https://doi.org/10.1126/science.1230473.

1109 32. Choi, U.B., Zhao, M., White, K.I., Pfuetzner, R.A., Esquivies, L., Zhou, Q., and Brunger,
1110 A.T. (2018). NSF-mediated disassembly of on- and off-pathway SNARE complexes and
1111 inhibition by complexin. eLife *7*, e36497. https://doi.org/10.7554/eLife.36497.

1112 33. Fasshauer, D., Bruns, D., Shen, B., Jahn, R., and Brunger, A.T. (1997). A Structural Change
1113 Occurs upon Binding of Syntaxin to SNAP-25. J. Biol. Chem. *272*, 4582–4590.
1114 https://doi.org/10.1074/jbc.272.7.4582.

1115 34. Misura, K.M.S., Gonzalez, L.C., May, A.P., Scheller, R.H., and Weis, W.I. (2001). Crystal
1116 Structure and Biophysical Properties of a Complex between the N-terminal SNARE Region
1117 of SNAP25 and Syntaxin 1a *. J. Biol. Chem. *276*, 41301–41309.
1118 https://doi.org/10.1074/jbc.M106853200.

1119 35. Weninger, K., Bowen, M.E., Choi, U.B., Chu, S., and Brunger, A.T. (2008). Accessory
1120 Proteins Stabilize the Acceptor Complex for Synaptobrevin, the 1:1 Syntaxin/SNAP-25
1121 Complex. Structure *16*, 308–320. https://doi.org/10.1016/j.str.2007.12.010.

1122 36. Hesselbarth, J., and Schmidt, C. (2023). Mass spectrometry uncovers intermediates and off-
1123 pathway complexes for SNARE complex assembly. Commun. Biol. *6*, 1–15.
1124 https://doi.org/10.1038/s42003-023-04548-0.

1125 37. Hayashi, T., McMahon, H., Yamasaki, S., Binz, T., Hata, Y., Südhof, T.C., and Niemann, H.
1126 (1994). Synaptic vesicle membrane fusion complex: action of clostridial neurotoxins on
1127 assembly. EMBO J. *13*, 5051–5061. https://doi.org/10.1002/j.1460-2075.1994.tb06834.x.

1128 38. Gao, Y., Khan, Y.A., Mo, W., White, K.I., Perkins, M., Pfuetzner, R.A., Trapani, J.G.,
1129 Brunger, A.T., and Nicolson, T. (2023). Sensory deficit screen identifies nsf mutation that
1130 differentially affects SNARE recycling and quality control. Cell Rep. *42*.
1131 https://doi.org/10.1016/j.celrep.2023.112345.

1132 39. Hayashi, T., Yamasaki, S., Nauenburg, S., Binz, T., and Niemann, H. (1995). Disassembly of
1133 the reconstituted synaptic vesicle membrane fusion complex in vitro. EMBO J. *14*, 2317–
1134 2325. https://doi.org/10.1002/j.1460-2075.1995.tb07226.x.

1135 40. Vivona, S., Cipriano, D.J., O'Leary, S., Li, Y.H., Fenn, T.D., and Brunger, A.T. (2013).
1136 Disassembly of All SNARE Complexes by N-Ethylmaleimide-sensitive Factor (NSF) Is
1137 Initiated by a Conserved 1:1 Interaction between α-Soluble NSF Attachment Protein (SNAP)
1138 and SNARE Complex. J. Biol. Chem. *288*, 24984–24991.
1139 https://doi.org/10.1074/jbc.M113.489807.

1140 41. Zhao, M., Wu, S., Zhou, Q., Vivona, S., Cipriano, D.J., Cheng, Y., and Brunger, A.T. (2015).
1141 Mechanistic insights into the recycling machine of the SNARE complex. Nature *518*, 61–67.
1142 https://doi.org/10.1038/nature14148.

1143 42. Nagiec, E.E., Bernstein, A., and Whiteheart, S.W. (1995). Each Domain of the N-
1144 Ethylmaleimide-sensitive Fusion Protein Contributes to Its Transport Activity (*). J. Biol.
1145 Chem. *270*, 29182–29188. https://doi.org/10.1074/jbc.270.49.29182.

1146 43. Matveeva, E.A., He, P., and Whiteheart, S.W. (1997). N-Ethylmaleimide-sensitive Fusion
1147 Protein Contains High and Low Affinity ATP-binding Sites That Are Functionally Distinct *.
1148 J. Biol. Chem. *272*, 26413–26418. https://doi.org/10.1074/jbc.272.42.26413.

1149 44. Xiao, W., Poirier, M.A., Bennett, M.K., and Shin, Y.-K. (2001). The neuronal t-SNARE
1150 complex is a parallel four-helix bundle. Nat. Struct. Biol. *8*, 308–311.
1151 https://doi.org/10.1038/86174.

1152 45. Margittai, M., Fasshauer, D., Pabst, S., Jahn, R., and Langen, R. (2001). Homo- and
1153 Heterooligomeric SNARE Complexes Studied by Site-directed Spin Labeling *. J. Biol.
1154 Chem. *276*, 13169–13177. https://doi.org/10.1074/jbc.M010653200.

1155 46. Lai, Y., Choi, U.B., Leitz, J., Rhee, H.J., Lee, C., Altas, B., Zhao, M., Pfuetzner, R.A., Wang,
1156 A.L., Brose, N., et al. (2017). Molecular Mechanisms of Synaptic Vesicle Priming by
1157 Munc13 and Munc18. Neuron *95*, 591-607.e10.
1158 https://doi.org/10.1016/j.neuron.2017.07.004.

1159 47. Stepien, K.P., Xu, J., Zhang, X., Bai, X.-C., and Rizo, J. (2022). SNARE assembly
1160 enlightened by cryo-EM structures of a synaptobrevin–Munc18-1–syntaxin-1 complex. Sci.
1161 Adv. *8*, eabo5272. https://doi.org/10.1126/sciadv.abo5272.

1162 48. Sanyal, S., and Krishnan, K.S. (2001). Lethal comatose mutation in Drosophila reveals
1163 possible role for NSF in neurogenesis. NeuroReport *12*, 1363.

1164 49. Ernst, J.A., and Brunger, A.T. (2003). High Resolution Structure, Stability, and
1165 Synaptotagmin Binding of a Truncated Neuronal SNARE Complex *. J. Biol. Chem. *278*,
1166 8630–8636. https://doi.org/10.1074/jbc.M211889200.

1167 50. de la Peña, A.H., Goodall, E.A., Gates, S.N., Lander, G.C., and Martin, A. (2018). Substrate-
1168 engaged 26S proteasome structures reveal mechanisms for ATP-hydrolysis–driven
1169 translocation. Science *362*, eaav0725. https://doi.org/10.1126/science.aav0725.

1170 51. Punjani, A., and Fleet, D.J. (2021). 3D variability analysis: Resolving continuous flexibility
1171 and discrete heterogeneity from single particle cryo-EM. J. Struct. Biol. *213*, 107702.
1172 https://doi.org/10.1016/j.jsb.2021.107702.

1173 52. Khan, Y.A., White, K.I., Pfuetzner, R.A., Singal, B., Esquivies, L., Mckenzie, G., Liu, F.,
1174 DeLong, K., Choi, U.B., Montabana, E., et al. (2024). Sec18 side-loading is essential for
1175 universal SNARE recycling across cellular contexts. Preprint at bioRxiv,
1176 https://doi.org/10.1101/2024.08.30.610324 https://doi.org/10.1101/2024.08.30.610324.

1177 53. Zhou, H., Di Palma, S., Preisinger, C., Peng, M., Polat, A.N., Heck, A.J.R., and Mohammed,
1178 S. (2013). Toward a Comprehensive Characterization of a Human Cancer Cell
1179 Phosphoproteome. J. Proteome Res. *12*, 260–271. https://doi.org/10.1021/pr300630k.

1180 54. Zhou, Q., Zhou, P., Wang, A.L., Wu, D., Zhao, M., Südhof, T.C., and Brunger, A.T. (2017).
1181 The primed SNARE–complexin–synaptotagmin complex for neuronal exocytosis. Nature
1182 *548*, 420–425. https://doi.org/10.1038/nature23484.

1183 55. Zhou, Q., Lai, Y., Bacaj, T., Zhao, M., Lyubimov, A.Y., Uervirojnangkoorn, M., Zeldin, O.B.,
1184 Brewster, A.S., Sauter, N.K., Cohen, A.E., et al. (2015). Architecture of the synaptotagmin–
1185 SNARE machinery for neuronal exocytosis. Nature *525*, 62–67.
1186 https://doi.org/10.1038/nature14975.

1187 56. Smith, G.R., Contreras-Moreira, B., Zhang, X., and Bates, P.A. (2004). A link between
1188 sequence conservation and domain motion within the AAA+ family. J. Struct. Biol. *146*,
1189 189–204. https://doi.org/10.1016/j.jsb.2003.11.022.

1190 57. Khan, Y.A., White, K.I., and Brunger, A.T. (2022). The AAA+ superfamily: a review of the
1191 structural and mechanistic principles of these molecular machines. Crit. Rev. Biochem. Mol.
1192 Biol. *57*, 156–187. https://doi.org/10.1080/10409238.2021.1979460.

1193 58. Huang, X., Sun, S., Wang, X., Fan, F., Zhou, Q., Lu, S., Cao, Y., Wang, Q.-W., Dong, M.-Q.,
1194 Yao, J., et al. (2019). Mechanistic insights into the SNARE complex disassembly. Sci. Adv.
1195 *5*, eaau8164. https://doi.org/10.1126/sciadv.aau8164.

1196 59. Greaves, J., Gorleku, O.A., Salaun, C., and Chamberlain, L.H. (2010). Palmitoylation of the
1197 SNAP25 Protein Family. J. Biol. Chem. *285*, 24629–24638.
1198 https://doi.org/10.1074/jbc.M110.119289.

1199 60. Jumper, J., Evans, R., Pritzel, A., Green, T., Figurnov, M., Ronneberger, O.,
1200 Tunyasuvunakool, K., Bates, R., Žídek, A., Potapenko, A., et al. (2021). Highly accurate
1201 protein structure prediction with AlphaFold. Nature *596*, 583–589.
1202 https://doi.org/10.1038/s41586-021-03819-2.

1203 61. Croll, T.I. (2018). ISOLDE: a physically realistic environment for model building into low-
1204 resolution electron-density maps. Acta Crystallogr. Sect. Struct. Biol. *74*, 519–530.
1205 https://doi.org/10.1107/S2059798318002425.

1206 62. Schneider, C.A., Rasband, W.S., and Eliceiri, K.W. (2012). NIH Image to ImageJ: 25 years
1207 of image analysis. Nat. Methods *9*, 671–675. https://doi.org/10.1038/nmeth.2089.

1208 63. Cipriano, D.J., Jung, J., Vivona, S., Fenn, T.D., Brunger, A.T., and Bryant, Z. (2013).
1209 Processive ATP-driven Substrate Disassembly by the N-Ethylmaleimide-sensitive Factor
1210 (NSF) Molecular Machine♦. J. Biol. Chem. *288*, 23436–23445.
1211 https://doi.org/10.1074/jbc.M113.476705.

1212 64. Studier, F.W. (2005). Protein production by auto-induction in high-density shaking cultures.
1213 Protein Expr. Purif. *41*, 207–234. https://doi.org/10.1016/j.pep.2005.01.016.

1214 65. Mastronarde, D.N. (2005). Automated electron microscope tomography using robust
1215 prediction of specimen movements. J. Struct. Biol. *152*, 36–51.
1216 https://doi.org/10.1016/j.jsb.2005.07.007.

66. Zheng, S.Q., Palovcak, E., Armache, J.-P., Verba, K.A., Cheng, Y., and Agard, D.A. (2017). MotionCor2 - anisotropic correction of beam-induced motion for improved cryo-electron microscopy. Nat. Methods *14*, 331–332. https://doi.org/10.1038/nmeth.4193.

67. Rohou, A., and Grigorieff, N. (2015). CTFFIND4: Fast and accurate defocus estimation from electron micrographs. J. Struct. Biol. *192*, 216–221. https://doi.org/10.1016/j.jsb.2015.08.008.

68. Scheres, S.H.W. (2012). RELION: Implementation of a Bayesian approach to cryo-EM structure determination. J. Struct. Biol. *180*, 519–530. https://doi.org/10.1016/j.jsb.2012.09.006.

69. Zivanov, J., Nakane, T., Forsberg, B.O., Kimanius, D., Hagen, W.J., Lindahl, E., and Scheres, S.H. (2018). New tools for automated high-resolution cryo-EM structure determination in RELION-3. eLife *7*, e42166. https://doi.org/10.7554/eLife.42166.

70. Punjani, A., Rubinstein, J.L., Fleet, D.J., and Brubaker, M.A. (2017). cryoSPARC: algorithms for rapid unsupervised cryo-EM structure determination. Nat. Methods *14*, 290–296. https://doi.org/10.1038/nmeth.4169.

71. Pintilie, G.D., Zhang, J., Goddard, T.D., Chiu, W., and Gossard, D.C. (2010). Quantitative analysis of cryo-EM density map segmentation by watershed and scale-space filtering, and fitting of structures by alignment to regions. J. Struct. Biol. *170*, 427–438. https://doi.org/10.1016/j.jsb.2010.03.007.

72. Pettersen, E.F., Goddard, T.D., Huang, C.C., Couch, G.S., Greenblatt, D.M., Meng, E.C., and Ferrin, T.E. (2004). UCSF Chimera—A visualization system for exploratory research and analysis. J. Comput. Chem. *25*, 1605–1612. https://doi.org/10.1002/jcc.20084.

73. Emsley, P., Lohkamp, B., Scott, W.G., and Cowtan, K. (2010). Features and development of Coot. Acta Crystallogr. D Biol. Crystallogr. *66*, 486–501. https://doi.org/10.1107/S0907444910007493.

74. Goddard, T.D., Huang, C.C., Meng, E.C., Pettersen, E.F., Couch, G.S., Morris, J.H., and Ferrin, T.E. (2018). UCSF ChimeraX: Meeting modern challenges in visualization and analysis. Protein Sci. *27*, 14–25. https://doi.org/10.1002/pro.3235.

75. Adams, P.D., Afonine, P.V., Bunkóczi, G., Chen, V.B., Davis, I.W., Echols, N., Headd, J.J., Hung, L.-W., Kapral, G.J., Grosse-Kunstleve, R.W., et al. (2010). PHENIX: a comprehensive Python-based system for macromolecular structure solution. Acta Crystallogr. D Biol. Crystallogr. *66*, 213–221. https://doi.org/10.1107/S0907444909052925.

76. Afonine, P.V., Poon, B.K., Read, R.J., Sobolev, O.V., Terwilliger, T.C., Urzhumtsev, A., and Adams, P.D. (2018). Real-space refinement in PHENIX for cryo-EM and crystallography. Acta Crystallogr. Sect. Struct. Biol. *74*, 531–544. https://doi.org/10.1107/S2059798318006551.

77. Yu, R.C., Jahn, R., and Brunger, A.T. (1999). NSF N-Terminal Domain Crystal Structure: Models of NSF Function. Mol. Cell *4*, 97–107. https://doi.org/10.1016/S1097-2765(00)80191-4.

78. Joosten, R.P., Long, F., Murshudov, G.N., and Perrakis, A. (2014). The PDB_REDO server for macromolecular structure model optimization. IUCrJ *1*, 213–220. https://doi.org/10.1107/S2052252514009324.

79. Hamelryck, T., and Manderick, B. (2003). PDB file parser and structure class implemented in Python. Bioinformatics *19*, 2308–2310. https://doi.org/10.1093/bioinformatics/btg299.

80. Cock, P.J.A., Antao, T., Chang, J.T., Chapman, B.A., Cox, C.J., Dalke, A., Friedberg, I., Hamelryck, T., Kauff, F., Wilczynski, B., et al. (2009). Biopython: freely available Python tools for computational molecular biology and bioinformatics. Bioinformatics *25*, 1422–1423. https://doi.org/10.1093/bioinformatics/btp163.

81. McKinney, W. (2010). Data Structures for Statistical Computing in Python. In Proceedings of the 9th Python in Science Confference, pp. 56–61. https://doi.org/10.25080/Majora-92bf1922-00a.

82. Harris, C.R., Millman, K.J., van der Walt, S.J., Gommers, R., Virtanen, P., Cournapeau, D., Wieser, E., Taylor, J., Berg, S., Smith, N.J., et al. (2020). Array programming with NumPy. Nature *585*, 357–362. https://doi.org/10.1038/s41586-020-2649-2.

83. Virtanen, P., Gommers, R., Oliphant, T.E., Haberland, M., Reddy, T., Cournapeau, D., Burovski, E., Peterson, P., Weckesser, W., Bright, J., et al. (2020). SciPy 1.0: fundamental algorithms for scientific computing in Python. Nat. Methods *17*, 261–272. https://doi.org/10.1038/s41592-019-0686-2.

84. Pedregosa, F., Varoquaux, G., Gramfort, A., Michel, V., Thirion, B., Grisel, O., Blondel, M., Prettenhofer, P., Weiss, R., Dubourg, V., et al. (2011). Scikit-learn: Machine Learning in Python. J. Mach. Learn. Res. *12*, 2825–2830.

85. Hunter, J.D. (2007). Matplotlib: A 2D Graphics Environment. Comput. Sci. Eng. *9*, 90–95. https://doi.org/10.1109/MCSE.2007.55.

86. Gowers, R.J., Linke, M., Barnoud, J., Reddy, T.J.E., Melo, M.N., Seyler, S.L., DomaÅ„ski, J., Dotson, D.L., Buchoux, S., Kenney, I.M., et al. (2016). MDAnalysis: A Python Package for the Rapid Analysis of Molecular Dynamics Simulations. In Proceedings of the 15th Python in Science Conference, S. Benthall and S. Rostrup, eds., pp. 98–105. https://doi.org/10.25080/Majora-629e541a-00e.